

RESEARCH PAPER

Immunosuppression with cyclosporine versus tacrolimus shows distinctive nephrotoxicity profiles within renal compartments

Hasan Demirci^{1,2}  | Suncica Popovic¹  | Carsten Dittmayer³ | Duygu Elif Yilmaz¹  | Ismail Amr El-Shimy⁴ | Michael Mülleder⁵ | Christian Hinze⁶ | Mingzhen Su² | Philipp Mertins⁷ | Marieluise Kirchner⁷ | Bilgin Osmanodja⁸ | Alexander Paliege⁹ | Klemens Budde⁸ | Kerstin Amann¹⁰ | Pontus B. Persson¹¹ | Kerim Mutig^{11,12} | Sebastian Bachmann^{1,2}

¹Institute of Functional Anatomy, Charité, Universitätsmedizin Berlin, Berlin, Germany

²Department of Cell- and Neurobiology, Charité, Universitätsmedizin Berlin, Berlin, Germany

³Department of Neuropathology, Charité, Universitätsmedizin Berlin, Berlin, Germany

⁴Molecular Epidemiology Unit, Berlin Institute of Health, Charité, Universitätsmedizin Berlin, Berlin, Germany

⁵Core Facility-High-Throughput Mass Spectrometry, Charité, Universitätsmedizin Berlin, Berlin, Germany

⁶Department of Nephrology and Hypertension, Hannover Medical School, Hannover, Germany

⁷Core Unit Proteomics, Berlin Institute of Health at Charité, Universitätsmedizin Berlin and Max-Delbrück-Center for Molecular Medicine, Berlin, Germany

⁸Department of Nephrology and Medical Intensive Care, Charité Universitätsmedizin Berlin, Berlin, Germany

⁹Department of Nephrology, Universitätsklinikum Carl Gustav Carus Dresden, Dresden, Germany

¹⁰Department of Nephropathology, Institute of Pathology, University Hospital Erlangen, Friedrich-Alexander University Erlangen-Nuremberg, Erlangen, Germany

¹¹Department of Translational Physiology, Charité, Universitätsmedizin Berlin, Berlin, Germany

¹²Department of Pharmacology, Institute of Pharmacy, I.M. Sechenov First Moscow State Medical University, Moscow, Russia

Correspondence

Sebastian Bachmann, Department of Cell- and Neurobiology, Charité Universitätsmedizin Berlin, Campus Mitte, Charitéplatz 1, Berlin 10117, Germany.
Email: sbachm@charite.de

Funding information

Deutsche Forschungsgemeinschaft BA700/22-2; SFB 1365-C04/-S01; MU2924/2-2

Abstract

Aim: Calcineurin inhibitors (CNIs) are the backbone for immunosuppression after solid organ transplantation. Although successful in preventing kidney transplant rejection, their nephrotoxic side effects contribute to allograft injury. Renal parenchymal lesions occur for cyclosporine A (CsA) as well as for the currently favored tacrolimus (Tac). We aimed to study whether chronic CsA and Tac exposures, before reaching irreversible nephrotoxic damage, affect renal compartments differentially and whether related pathogenic mechanisms can be identified.

Methods: CsA and Tac were administered chronically in wild type Wistar rats using osmotic minipumps over 4 weeks. Functional parameters were controlled.

This is an open access article under the terms of the [Creative Commons Attribution](https://creativecommons.org/licenses/by/4.0/) License, which permits use, distribution and reproduction in any medium, provided the original work is properly cited.

© 2024 The Author(s). *Acta Physiologica* published by John Wiley & Sons Ltd on behalf of Scandinavian Physiological Society.

Electron microscopy, confocal, and 3D-structured illumination microscopy were used for histopathology. Clinical translatability was tested in human renal biopsies. Standard biochemical, RNA-seq, and proteomic technologies were applied to identify implicated molecular pathways.

Results: Both drugs caused significant albeit differential damage in vasculature and nephron. The glomerular filtration barrier was more affected by Tac than by CsA, showing prominent deteriorations in endothelium and podocytes along with impaired VEGF/VEGFR2 signaling and podocyte-specific gene expression. By contrast, proximal tubule epithelia were more severely affected by CsA than by Tac, revealing lysosomal dysfunction, enhanced apoptosis, impaired proteostasis and oxidative stress. Lesion characteristics were confirmed in human renal biopsies.

Conclusion: We conclude that pathogenetic alterations in the renal compartments are specific for either treatment. Considering translation to the clinical setting, CNI choice should reflect individual risk factors for renal vasculature and tubular epithelia. As a step in this direction, we share protein signatures identified from multiomics with potential pathognomonic relevance.

KEYWORDS

calcineurin inhibitor nephropathy, multiomics, pore endothelium, proximal tubule, unfolded protein response, VEGF

1 | INTRODUCTION

Calcineurin inhibitors (CNIs) such as cyclosporine A (CsA) and tacrolimus (Tac, FK506) have become the basis for immunosuppressive treatment in organ transplant recipients and patients with autoimmune diseases over the past four decades. Today, over 90% of kidney transplant recipients in Western countries are maintained on CNI-containing immunosuppressive regimens. Apart from a satisfactory outcome at short term, chronic use of CNI causes nephrotoxicity in a significant proportion of renal and nonrenal transplant recipients, affecting renal function.¹⁻³ CNI elimination or substitution with other immunosuppressant regimens have been explored, but CNI alternatives are widely considered inferior.^{1,4,5} CNI nephrotoxicity with decreasing allograft function may root from chronic hypoperfusion related to hyaline arteriolopathy with glomerular scarring or direct tubular toxicity. Their interplay leads to interstitial fibrosis/tubular atrophy (IF/TA). Immunological damage and comorbidities unrelated to CNI add to potential CNI injury. Thus, whether certain pathological landmarks occur specifically for CsA or Tac remains to be determined.^{2,6-8} Calcineurin is a calcium/calmodulin-dependent serine–threonine phosphatase notable for its key role in T cell function. Upon activation, it dephosphorylates and thereby activates transcription factors of the NFAT (nuclear factor of activated T-cells) family. NFAT induce expression of key genes for T-lymphocyte differentiation.^{9,10} Calcineurin and NFAT isoforms are, however, not

T-cell specific and may encompass interactions with other substrates beyond immunology. CNI nephrotoxicity can thus involve vasoconstriction, hypertension, tissue hypoxia, oxidative stress, anemia, hyperkalemia, metabolic acidosis, dysregulation of major endo- and paracrine systems, and metabolic stress.¹¹⁻¹⁵ Although widely assumed that CsA and Tac produce identical lesions,⁷ this view is not unopposed. CsA may cause greater nephrotoxicity than Tac.^{3,16,17} Both CNI inhibit calcineurin activity by forming complexes with distinct members of the immunophilin family, i.e. cyclophilins for CsA and FKBP12 for Tac.² This may explain the specific toxicity profiles of various CNIs. Distinctively, CsA affects proteostasis, since the chaperone activity of cyclophilins interacts with protein maturation.¹⁶ Studies comparing CsA versus Tac in cell culture consequently show stronger association of CsA with ER stress and the unfolded protein response (UPR), whereas Tac did not.¹⁷⁻²⁰ CsA nephrotoxicity may further involve altered JAK/STAT signaling and salt-sensitive mitochondrial dysfunction.²¹ In search of candidates for nephroprotection from CsA, transcription factor EB (TFEB)-mediated autophagy flux and lysosomal dysfunction are discussed, owing to CsA-induced mTOR overactivity.²² The current preference to provide Tac rather than CsA³ (except for new onset of diabetes cases¹ and specific combination therapies) requires substantiation. We test whether CsA and Tac exposure, before reaching irreversible nephrotoxic damage, affect renal compartments differently. We verify this in a translational approach by

retrospective analysis of human renal biopsies with CNI nephrotoxicity. We present distinctive pathogenic pathways and related mechanisms in Tac versus CsA serving to develop nephroprotective measures in patient immunosuppressive protocols.

2 | METHODS

2.1 | Animals

Animal experiments were approved by the German Animal Welfare Regulation Authorities for the protection of animals used for scientific purposes (Berlin Senate; G0148/18). Adult male Wistar rats (10–12 weeks old, 290 ± 21 g body weight [b.w.]) were divided into 4 groups (each $n=6$) receiving cyclosporine A (CsA, Sandimmun, Novartis) and the respective vehicle (Veh, saline), or tacrolimus (Tac, FK506, Selleckchem) and the respective vehicle (25% DMSO/75% PEG500, Sigma) via subcutaneously implanted osmotic minipumps (Alzet, 2ML4) for 28 days. Two separate sets of groups were treated, one for morphological, one for biochemical analysis. Various dosage levels (10–50 mg/kg b.w./d CsA, up to 6 mg/kg b.w./d Tac) were tested to determine optimal application by histology; resulting dosages were 30 mg CsA/kg b.w./d (target plasma trough level $3 \mu\text{g/mL}$) and 2 mg FK506/kg b.w./d (target plasma trough level 3.5 ng/mL). During housing, animals were kept in a 12-h day/night cycle, with ad libitum access to drinking water and standard rodent chow (Altromin 1324). For pump filling, 100 mg CsA and 7 mg Tac/mL of vehicle were used, respectively. For minipump implantation, rats were anesthetized by isoflurane inhalation. An incision of the neck skin was performed and the subcutaneous tissue dilated to create a pocket for the pump. The filled pump was then inserted into the pocket and the wound closed with metal clips. On the second last day of each experiment, rats were placed in metabolic cages for 24 h with water and chow ad libitum to collect urine. At the end of the experiments, rats were anesthetized with ketamin/xylavet (90/10 mg/kg BW; CP-Pharma) to obtain blood samples. Urine and blood samples were analyzed by a commercial laboratory (IMD Labor). For biochemical evaluation, one kidney was clamped and removed for biochemical analysis before perfusion fixation, or both kidneys were removed without fixation.

2.2 | Retrospective pathological analysis of human renal biopsies

The clinical and research activities being reported are consistent with the Principles of the Declaration of

Istanbul as outlined in the “Declaration of Istanbul on Organ Trafficking and Transplant Tourism.” All studies on human kidney tissue were approved by national and local research ethics committees. Adult recipients of an organ transplantation in the transplant centers of Charité Universitätsmedizin Berlin and Universitätsklinikum Carl Gustav Carus Dresden were included. The study was classified as part of an ongoing pathological investigation (Department of Nephropathology, University of Erlangen-Nürnberg) with no requirement of informed consent based on the local treatment contract providing retrospective anonymized analysis of samples. The study was undertaken in accordance with the Declaration of Helsinki. Cases were identified from the Charité nephrology database. Between January 2018 and December 2023 11 for-cause or protocol kidney biopsies were performed in these patients, analyzed according to BANFF 2019 and enrolled in the retrospective study. As inclusion criteria, established CNI nephrotoxicity was defined by a biopsy showing severe hyalinosis (ah2-3) in the absence of any other causes more likely to contribute to the diagnosis of severe hyalinosis such as poor transplant quality.²³ Young donors (<40 years of age, $n=7$) or living donors presumed to have an ah score of 0 at the time of transplantation were included. A total of 11 biopsies from 9 renal allograft recipients and 2 nonrenal transplant recipients was analyzed; in total, 4 were from patients receiving CsA and 7 receiving Tac. In 6 cases, successful conversion (increase of $>5 \text{ mL/min eGFR}$ after conversion) from CNI-based to belatacept-based immunosuppression was an additional selection criterion to confirm CNI nephrotoxicity.²⁴ Diabetes mellitus, hyperglycemia and rejection were exclusion criteria. Biopsy specimens had been processed with standard techniques in the Department of Nephropathology, University of Erlangen-Nürnberg. Histological and immunohistological staining, and electron microscopy had been analyzed by an experienced nephropathologist (K.A.). All Banff lesions were graded on a scale of 0–3, with higher scores indicating more severe abnormalities. Sections were reevaluated by light and electron microscopy for the present study. A votum of Charité ethics commission has been consented (Charité No. EA4/002/24).

2.3 | Blood and urine analysis

Blood from rats was taken from the inferior vena cava using heparinized syringes, decanted into Eppendorf tubes, left for 30 min at room temperature (RT), and centrifuged at $2000 \times g$ for 10 min at 4°C to obtain serum with the supernatant. Creatinine was measured and its clearance calculated using the formula, $\text{CrCl (mL/min)} = (\text{urine}$

creatinine [mg/dL] × urine flow [mL/min]/serum creatinine [mg/dL]). Fractional excretion of sodium (FeNa) was calculated using the formula, $\text{FeNa (\%)} = (\text{urinary sodium [mg/dL]} \times \text{serum creatinine [mg/dL]}) / (\text{serum sodium [mg/dL]} \times \text{urinary creatinine [mg/dL]})$.

2.4 | Perfusion fixation and tissue processing

Rat kidneys were perfused via the abdominal aorta, first with 3% hydroxyethyl starch in 0.1 M Na-cacodylate (Caco) for 20–30 s, then with 3% paraformaldehyde/3% hydroxyethyl starch in Caco for 5 min. For paraffin embedding, tissue was post-fixed in the same fixation solution overnight at 4°C, then transferred to Caco supplemented with 300 mOsm sucrose and 0.02% NaN₃ until embedding. For cryostat sectioning, tissue was transferred directly after perfusion to 800 mOsm sucrose in Caco at 4°C overnight, snap-frozen in 2-methyl butane cooled with liquid nitrogen, and stored at –80°C. For histology and immunohistochemistry (IHC), tissues were dehydrated and paraffin-embedded. For electron microscopy, tissues were post-fixed overnight at RT in 1.5% glutaraldehyde/1.5% paraformaldehyde containing 0.05% picric acid in Caco, then in 1% osmium tetroxide/0.8% potassium hexacyanoferrate in Caco for 1.5 h at RT for transmission electron microscopy (TEM) or in 1% aqueous osmium tetroxide for scanning electron microscopy (SEM). Tissues were then dehydrated and embedded in epoxy resin for semithin sectioning and light microscopy (LM) or ultrathin sectioning and TEM analysis using standard methodology. For SEM, samples were high pressure-critical point-dried and sputter-coated.

2.5 | Histology and immunostaining

For paraffin histology and IHC, 4 µm-thick sections were cut, mounted on glass slides, and deparaffinized. Histology was done using standard Periodic acid-Schiff (PAS), Masson's Trichrome, or Sirius Red staining protocols. For IHC, heat-induced epitope retrieval was generally performed for 6 min by cooking slides in citrate buffer (10 mM sodium citrate, pH 6.0) using a pressure cooker. Sections were blocked with 5% BSA (Serva) in TBS for 30 min at RT. Samples were then incubated overnight at 4°C with primary antibody dissolved in 1% BSA/TBS or blocking medium (antibodies listed in Table S1). After washing in TBS, fluorescently labeled secondary antibodies (Table S1) were dissolved in 1% BSA/TBS or blocking buffer and incubated for 1 h at RT. Sections were then mounted in PBS-glycerol (1:9). Nuclei were stained with

DAPI (Sigma). For immunoperoxidase staining, sections were incubated in methanol containing 0.3% hydrogen peroxide (H₂O₂) for 15 min, then in TBS, blocked in 5% BSA/TBS at 37°C for 30 min, and incubated with primary antibody at 4°C overnight, followed by HRP-conjugated secondary antibody diluted in 5% BSA/TBS for 1 h at RT. DAB (Sigma, D8001) containing 1% H₂O₂ was applied as a chromogen. Staining was monitored under LM; reaction was stopped by washing with TBS. Samples were then dehydrated in a graded ethanol series, cleared with xylene, and mounted in Eukitt Quick-hardening mounting medium (Sigma).

2.6 | Light microscopy and image processing

Images were acquired using a Zeiss LSM 5 Exciter confocal microscope (LSM) equipped with Imager.M1 and a NeoFluar objective lens (63×/NA 1.40). The laser lines used were 405, 488, 543, and 633 nm. Fluorescence images were acquired, some of them with additional differential interference contrast (DIC) overlay. The system was operated with Zen 2008 software (Zeiss). Immunoperoxidase, PAS, Masson's trichrome, and Sirius red-stained sections were examined in bright-field microscopy under a Zeiss Axio Imager Z2 LM equipped with an ApoTome2 structured illumination acquisition system and a Plan-Apochromat 20×/0.8 objective using Zeiss ZEN 2012 software (blue edition). All image processing was done with ImageJ (NIH).

2.7 | Filtration slit density analysis

Rat kidney sections (2 µm) were deparaffinized and rehydrated, followed by boiling for 5 min in Tris-EDTA buffer (10 mmol/L Tris, 1 mmol/L EDTA, pH 9) in a pressure cooker for antigen retrieval. Next, sections were blocked in blocking solution (1% fetal bovine serum, 1% BSA, 0.1% fish gelatine, 1% normal goat serum) for 1 h. Primary antibodies (Table S1) were incubated overnight at 4°C. After washing three times in PBS, secondary antibodies (Table S1) were incubated for 1 h at RT. Nuclei were counterstained with DAPI for 5 min, followed by a washing step in PBS. Finally, the sections were washed in distilled H₂O and mounted in Mowiol 4–88 (Carl Roth) using high-precision cover glasses (Paul Marienfeld). The evaluation of the filtration slit density (FSD) was performed according to podocyte exact morphology measurement procedure (PEMP).^{25,26} 3D-structured illumination microscopy (3D-SIM) was performed with Z-stacks from 19 planes with 488 and 561 nm channels acquired from the

stained kidney sections using an N-SIM super-resolution microscope (Nikon) equipped with a 100x silicone objective. The Z-stacks were converted into a maximum intensity projection followed by the automatized identification of the filtration slit length as an index of foot process effacement. FSD was expressed as the ratio of the total filtration slit diaphragm per podocyte foot process area. FSD values of 20 glomeruli per animal were quantified in at least $n = 3$ rats per group.

2.8 | Electron microscopy

Samples from perfusion-fixed and post-fixed rat kidneys or immersion-fixed human kidney biopsies were embedded in Epon or, for rats only, transferred to critical-point drying for conventional TEM, large-scale scanning TEM (STEM), or SEM, respectively. Semithin sections (1 μm) were prepared from Epon blocks with an ultramicrotome (Ultracut E, Reichert-Jung) and stained with Richardson's stain for LM evaluation or to select a region for conventional or large-scale digitization. To screen pathological patterns ultrastructurally, conventional or large-scale ultrathin sections (200–400 nm) were prepared.²⁷ Sections for large-scale analysis were partly or completely digitized at 3–4 nm pixel size using TrakEM2 for stitching and nip2 for export to high-resolution tif files and inspection with QuPath. Qualitative and quantitative analyses were performed using either a Gemini 300 field emission scanning electron microscope (FESEM, Zeiss) equipped with a scanning transmission electron microscopy (STEM) detector, SmartSEM, and Atlas 5 software. Alternatively, a Zeiss EM901 was used for conventional TEM. For repository implementation on www.nanotomy.org and open access pan-and-zoom analysis, datasets were exported into a tiled, browser-based file format using Atlas 5 software. For conventional 3D-SEM, dried and sputter-coated samples were evaluated by FESEM using an SEM detector.

2.9 | Morphometric analysis

To assess tubulo-interstitial fibrosis from PAS-stained rat paraffin sections, brightness and contrast were adjusted in ImageJ. Lines were drawn around the perimeter of regions of interest (ROI); original magnification was 200 \times . Data were expressed as positively stained ROI versus selected field areas. All samples were examined in a blinded manner. For quantitative assessment of alpha-smooth muscle actin (α -SMA) and renin immunoperoxidase staining, at least 15 non-overlapping fields were selected and α -SMA- and renin-immunoreactive ROI evaluated using ImageJ. The average ratio of ROIs

to each microscopic field (200 \times magnification) was calculated and graphed. All measurements were performed by a single operator in a blinded fashion. Estimation of glomerular podocyte intactness was performed with anti-Wilms tumor 1 protein (WT1) immunofluorescence and DAPI staining using paraffin sections. Fluorescence signal was acquired on whole-slide images. Podocyte numbers per glomerulus were calculated from all glomeruli per section. Quantification of CD45-positive cells was performed with anti-CD45 immunofluorescence and DAPI staining using paraffin sections. The average number of CD45-positive cells was calculated by analyzing 10 non-overlapping fields at a magnification of 200 \times (high power field, HPF). Endothelial pore density was determined by counting the number of fenestrae per micrometer of glomerular basement membrane (GBM) in TEM images; total length of GBM was $>750 \mu\text{m}$ per animal. At least 6 glomeruli per animal were evaluated. To determine fenestration density of cortical peritubular capillaries, TEM images were used. The number of fenestrae per micrometer of basement membrane length was counted. Ten cross-sectional profiles per animal were evaluated; total length of basement membrane was $>850 \mu\text{m}$ per animal. Lysosome numbers in proximal tubules were counted per tubular area on Richardson's stained semithin plastic sections. Conventional lysosomes were termed "dark" based on their dark-blue stained core; those with clear-appearing cores were termed "heterolysosomes." Twelve to 15 fields selected randomly, each containing 3–4 proximal convoluted tubule (PCT) profiles, were examined at 200 \times magnification. The wall-to-lumen ratios of renal afferent arterioles were analyzed in PAS-stained paraffin sections. Only profiles with open lumen were chosen. Wall and lumen surface areas were calculated using ImageJ by drawing lines around outer and inner perimeter. Seven to 10 arterioles were studied per animal. The mean glomerular tuft area was measured by using anti-podocin-stained paraffin sections from entire kidneys imaged with the 3D-SIM. All available glomeruli with identifiable vascular pole were evaluated per section, their numbers ranging between 182 and 343. Podocin-immunoreactive area was quantified as μm^2 (NIPOKA). Quantification of anti-catalase immunofluorescence staining was performed by randomly selecting 10 optical fields, each containing 3–5 PCT profiles per slide at 200 \times magnification; proximal tubule was identified by DIC showing brush border membrane. Adjustments of pinhole, laser power, offset gain, and detector amplification below pixel saturation were maintained constant throughout. Mean fluorescence of catalase per PCT was determined with ImageJ. At least $n = 4$ to 6 rats per group were evaluated throughout except for FSD morphometric measurements ($n = 3$ rats).

2.10 | TUNEL assay

Deparaffinized rat kidney sections (4 μ m) were post-fixed in 4% PFA and labeled with TUNEL (Abcam, Ab66108) according to manufacturer's instructions in order to detect DNA fragmentation. Nuclei were counterstained with DAPI. Apoptotic signals were acquired by fluorescence microscopy (200 \times magnification) with DIC overlay. Labeled nuclei were counted in randomly chosen proximal tubular profiles from at least 10 adjacent optical fields and at least 15 randomly chosen glomeruli per animal, respectively. The apoptosis rate was calculated as the ratio of TUNEL-positive nuclei per total number of nuclei and field or glomerulus; $n = 5$ – 6 rats per group were used for each experiment. Image analysis was performed with ImageJ.

2.11 | Western blotting

Whole rat kidney tissue ($n = 6$ for each group) was ground in liquid nitrogen and lysed in homogenization buffer (250 mM sucrose, 10 mM triethanolamine [AppliChem, PanReac, ITW Reagents]), supplemented with a protease inhibitor cocktail (cOmplete™, Roche), and sonicated 4 times for 1 s each. The supernatant of the protein lysates was obtained by centrifugation at 1000g for 10 min at +4°C. Protein concentrations were measured using Micro BCA™ protein-assay-kit (Thermo Scientific). Samples were stored at -80°C until further processing. Samples were then mixed 1:4 with 4 \times Laemmli buffer (Bio-Rad) containing 10% (v/v) β -mercaptoethanol (Merck), incubated at 65°C for 10 min, separated by SDS PAGE (10% or 14%; 30 to 40 μ g per lane), and transferred to a PVDF membrane (Macherey-Nagel). Membranes were then blocked with 5% milk or BSA in TBS and incubated with primary antibody overnight at +4°C on a rotating wheel. Antibodies used for immunoblotting are listed in Table S1. HRP-conjugated secondary antibody (Dako; diluted 1:2000) was applied for 1 h at RT. Signal was generated by chemiluminescent reagent (Amersham ECL Western blotting detection reagent, GE Healthcare). Blots were imaged using an Intas ECL ChemoCam Imager (Intas Science Imaging). Densitometric quantification was performed using ImageJ.

2.12 | Angiotensin II ELISA assay

Rat plasma angiotensin II concentrations were measured using Angiotensin II EIA Kit (RAB0010, Sigma-Aldrich) according to manufacturer's instructions. Briefly, 100 μ L

of anti-Ang II antibody was added to each well and incubated overnight at +4°C. After a washing step, 100 μ L of plasma (four times diluted) or standard samples containing 20 pg/mL of biotinylated Ang II were added to the wells and incubated overnight at +4°C. After washing, 100 μ L of HRP-streptavidin solution was added to each well and incubated for 45 min, then 100 μ L of TMB substrate reagent was added. After 30 min of incubation in dark with gentle shaking in RT, 50 μ L of stop solution was added to each well and optical absorbance was read at 450 nm. Assays were done in duplicate.

2.13 | Quantitative polymerase chain reaction

cDNA synthesis was performed using 1 μ g of total rat kidney RNA ($n = 6$ for each group) with Tetro Reverse Transkriptase kit (Bioline GmbH). Quantitative polymerase chain reaction was performed using the QuantStudio 3 System Real-Time PCR instrument (Thermo Fisher Scientific) and HOT FIREPol EvaGreen qPCR Mix (Solis BioDyne). Primers were designed using the primer-BLAST program (<https://www.ncbi.nlm.nih.gov/tools/primer-blast/index>) and obtained from Metabion GmbH. All primers are listed in Table S2. The polymerase chain reaction protocol consisted of a 10-min holding step at 95°C and 40 cycles of 15 s at 95°C and 1 min at 60°C. The $\Delta\Delta\text{Ct}$ method was used for gene expression analysis and expression was normalized against β -actin.

2.14 | RNA extraction and qualification

Whole rat kidney total RNA was isolated using PeqGOLD TriFast (VWR Life SCIENCE) according to manufacturer's instructions. The purity of RNA was checked using NanoPhotometer R spectrophotometer (IMPLEN). Next, an RNA Nano 6000 Assay Kit and Bioanalyzer 2100 system (Agilent Technologies) were used to evaluate quantity and integrity of RNA.

2.15 | RNA sequencing and data processing

RNA sequencing (RNA-seq) of rat kidney RNA samples ($n = 4$ to 6 per group) was performed (Novogene, <https://en.novogene.com/>). A total amount of 1 μ g RNA per sample was used as input material. Sequencing libraries were generated using NEBNext RNA Library Prep Kit for Illumina (New England BioLabs), and index codes were

added to attribute sequences to each sample. Clustering of the index-coded samples was performed on a cBot Cluster Generation System with PE Cluster Kit cBot-HS (Illumina). After cluster generation, libraries were sequenced using Novaseq HisEquation 4000 platform (Illumina) and 150 bp paired-end reads were generated. Differential expression analysis between two groups was performed using DESeq2 R package. The resulting p values were adjusted using Benjamini and Hochberg's approach for controlling the False Discovery Rate (FDR). Genes with an adjusted p value < 0.1 (with no logFC cutoff) found by DESeq2 were considered as differentially expressed genes (DEG). RNA-seq data were deposited in the NCBI's Gene Expression Omnibus repository (GSE225215).

2.16 | Global proteomics

Global proteomics was performed by using protein lysates of rat kidneys ($n=4$ to 6 per group) according to a previously established methodology (Charité Core Facility for High Throughput Mass Spectrometry, Berlin).²⁸ Briefly, protein lysates were trypsinized followed by analyzing tryptic peptides by LC-MS/MS using a timsTOF Pro 2 mass spectrometer (Bruker). The raw data were processed using DIA-NN 1.8²⁹ with standard settings using MS1 and MS2 resolution of 10 ppm. Peptides were identified by library-free mode using the *Rattus norvegicus* UniProt (UniProt Consortium 2019) sequence database (UP000002494_10116, downloaded on 20210116) and the matched-between-runs (MBR) option. The output was filtered at 0.01 FDR at the peptide level. All further analyses were performed using the R package DEP.³⁰ Proteins with an adjusted p value < 0.1 (with no logFC cutoff) were considered as differentially expressed protein (DEP). Data are deposited in the ProteomeXchange Consortium via the PRIDE partner repository with an accession number: PXD038841.

2.17 | Global phosphoproteomics

Global phosphoproteomic analyses were performed³¹ using cryo-pulverized rat kidney tissues ($n=4-5$ per group) (Proteomics/Max Delbrück Center, Berlin). Samples were lysed in SDC lysis buffer (1% Na-deoxycholate, 150mM NaCl, 50mM Tris-HCl pH8.0, 1mM EDTA, 10mM DTT, 40mM CAA [2-chloroacetamide, Sigma], phosphatase inhibitor cocktail II and III [Sigma]) by heating to 95°C for 10 min. The solution was then cooled to RT, and Benzonase® (Merck; 50 units) was added for 30 min at 37°C. Protein (200µg per sample) was digested overnight at 37°C with endopeptidase LysC (Wako) and sequence-grade trypsin (Promega) at a 1:100 enzyme-to-protein ratio. Cleaned-up

peptides were labeled with TMTpro reagents (CsA sample set) or TMT10 (Tac sample set) according to manufacturer's protocols (Thermo Fisher Scientific). TMT labeled peptides of each experiment were combined, fractionated using high pH-reversed phase chromatography, and pooled into 15 fractions, which were used for phosphopeptide enrichment using immobilized metal affinity chromatography (IMAC). IMAC elutes were dried resolved in 3% acetonitrile / 0.1% formic acid, and separated on a high-performance liquid chromatography system (Thermo Fisher Scientific), which was coupled to a Q-Exactive HF-X instrument (Thermo Fisher Scientific). The mass spectrometer was operated in data-dependent acquisition mode. Raw data were analyzed using v 1.6.10.44 MaxQuant software package.³² The internal Andromeda search engine was used to search MS2 spectra against a decoy rat UniProt database (release 2019-07) containing forward and reverse sequences. The FDR was set to 1% for peptide and protein identifications, respectively. Unique and razor peptides were included for quantification. Statistical analysis was done with the Perseus software (version 1.6.2.1). Differentially expressed phosphoprotein (DEPP) were calculated using Student's t -test with FDR based cutoff of 5%. The data presented in the study are deposited in the ProteomeXchange Consortium via the PRIDE partner repository, accession number PXD038546.

2.18 | Gene ontology and pathway analyses

The gene ontology (GO) and pathway analyses for differentially expressed genes, proteins and phosphoproteins were performed using online bioinformatics tool Enrichr (<https://maayanlab.cloud/Enrichr/>). Pathways with a significance of $p < 0.05$ were defined as significantly regulated.

2.19 | Statistical analyses

Evaluations were done in an observer-blinded way. Statistical analysis was performed with GraphPad Prism 8 software. Normal distribution was tested using the Shapiro-Wilk test. If data were normally distributed, ordinary one-way analysis of variance was used for multiple groups, followed by Tukey's post-hoc test. For data that did not follow a normal distribution, the nonparametric Kruskal-Wallis test with Dunn's post-hoc test was used. Comparative analysis between two groups was performed by Student's t -test (normal distribution) or Mann-Whitney U -test (no normal distribution). A significance level of $p < 0.05$ was considered statistically significant; ns, not significant.

3 | RESULTS

3.1 | Physiologic parameters

CsA and Tac were delivered during 4 weeks by osmotic minipumps at established dosages.^{33,34} CNI-induced kidney injury was assessed by reduced creatinine clearance, elevated blood urea nitrogen (BUN) and cystatin C levels, and reduced fractional Na⁺ excretion (Table 1, Figure 1A–C). Final body weight in Tac was reduced by roughly 10%, eventually related with intermittent, mild diarrhea. Further variables are presented (Table 1).

3.2 | Overview pathology

Substantial pathological changes took place in CNI-recipient kidneys, which ranged between mild onset stages

and nephron destruction, reflecting CNI nephropathy. Mild-to-severe glomerular and tubulo-interstitial degenerative alterations were observed focally. Foci consisted of 5 to 20 tubular profiles, but also larger areas measuring up to 150.000 μm² were encountered. These were frequent in the subcapsular location but also extended to deeper parts of cortex and outer medulla, featuring onset striped fibrosis (Figure 1D). Mean proportional area occupied by foci was 4.0 ± 1.7% for CsA and 4.5 ± 1.3% in Tac; ns. Glomeruli adjacent to foci often displayed a retracted, albeit fully perfused phenotype. Interstitium of the foci was loose and meshwork-like in CsA, but dense and cell-enriched in Tac; fibrosis was illustrated by Trichrome and Sirius red staining (Figure 1E,F). α-SMA-immunoreactive signal suggested intensive profibrotic myofibroblast transdifferentiation near atrophic or necrotic tubules and adjacent glomeruli, vascular pericyte activation, and glomerular pericapsular activation, more intensely in CsA than in Tac

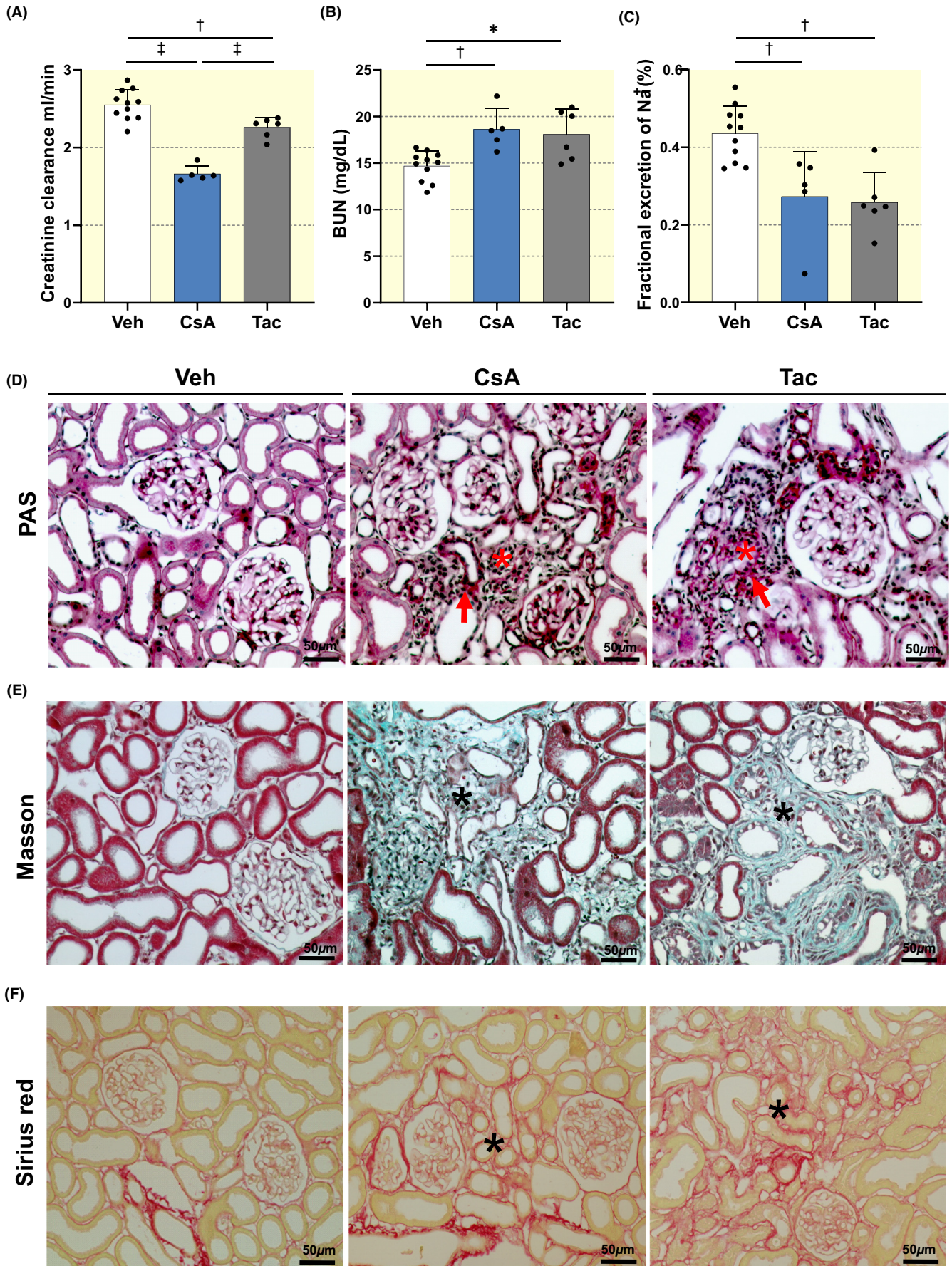
Parameter	Veh (n = 11)	CsA (n = 5)	Tac (n = 6)
Serum			
Na ⁺ (mmol/L)	142 ± 4	142 ± 1	143 ± 1
K ⁺ (mmol/L)	4.63 ± 0.82	4.50 ± 0.45	4.70 ± 0.53
Ca ²⁺ (mg/dL)	10.0 ± 0.7	9.70 ± 0.9	10.1 ± 0.3
Phosphate (mg/dL)	8.62 ± 0.96	8.09 ± 0.49	8.41 ± 0.54
Urea (mg/dL)	31.7 ± 3.80	40.0 ± 4.80*	38.70 ± 5.80**
Creatinine (mg/dL)	0.29 ± 0.02	0.33 ± 0.02*	0.32 ± 0.01**
Cystatin C (mg/L)	0.39 ± 0.06	0.53 ± 0.04*	0.49 ± 0.07**
Ang II (pg/mL)	154 ± 18	339 ± 38*	428 ± 108**
Trough level (ng/mL)	-	3040 ± 126	3.42 ± 0.80
Urine			
Na ⁺ (mmol/mg)	0.19 ± 0.03	0.11 ± 0.04*	0.11 ± 0.03**
K ⁺ (mmol/mg)	0.41 ± 0.04	0.47 ± 0.03	0.49 ± 0.06**
Urea (mg/mg)	61.0 ± 7.73	68.7 ± 6.44	76.1 ± 10.2**
Creatinine (mg/dL)	59.5 ± 19.7	56.6 ± 12.9	50.9 ± 11.6
Albumin (mg/mg)	0.005 ± 0.002	0.007 ± 0.003	0.006 ± 0.003
Urine flow (mL/24h)	19.2 ± 5.70	14.3 ± 3.30	21.3 ± 5.50
Osmolality (mOsm/kg)	1432 ± 346	1663 ± 269	1489 ± 215
Body weight (g)	385 ± 40	389 ± 26***	340 ± 8****

Note: Means ± SD, normalized by urine creatinine. Urine and blood parameters were obtained from rats after 4 weeks of treatment with vehicle (Veh), cyclosporine A (CsA), or tacrolimus (Tac).

p* < 0.05 when comparing Veh with CsA. *p* < 0.05 when comparing Veh with Tac. ****p* < 0.05 when comparing CsA with Tac.

TABLE 1 Physiologic parameters, numerical values.

FIGURE 1 Physiologic parameters and histological overview. Creatinine clearance (A), blood urea nitrogen (BUN, B), fractional sodium excretion (C), obtained from rats after 4 weeks of vehicle (Veh)-, cyclosporine A (CsA)-, or tacrolimus (Tac)-treatment (*n* = 5–11); means ± SD; **p* < 0.05; †*p* < 0.01; ‡*p* < 0.001. (D) Representative overviews of fibrotic foci (asterisk) in CsA and Tac; periodic acid-Schiff (PAS). Note thickening of peritubular basement membrane (arrow). (E) Green signal characterizes fibrotic foci (asterisks) in CsA and Tac (Masson's trichrome staining). (F) Sirius red staining indicates collagen deposits in fibrotic foci (asterisks) of CsA and Tac. Bars indicate magnification.



despite similar mean extension of signal (% area increases 20-fold in CsA, 18-fold in Tac; $p < 0.001$; [Figure S1A,B](#)). Inflammation was detected by CD45-positive leukocytes accumulating in fibrotic foci of CsA and Tac samples to similar extent (increases 2.4-fold in CsA, 2.8-fold in Tac; $p < 0.001$; [Figure S1C,D](#)).

3.3 | Renal vasculature

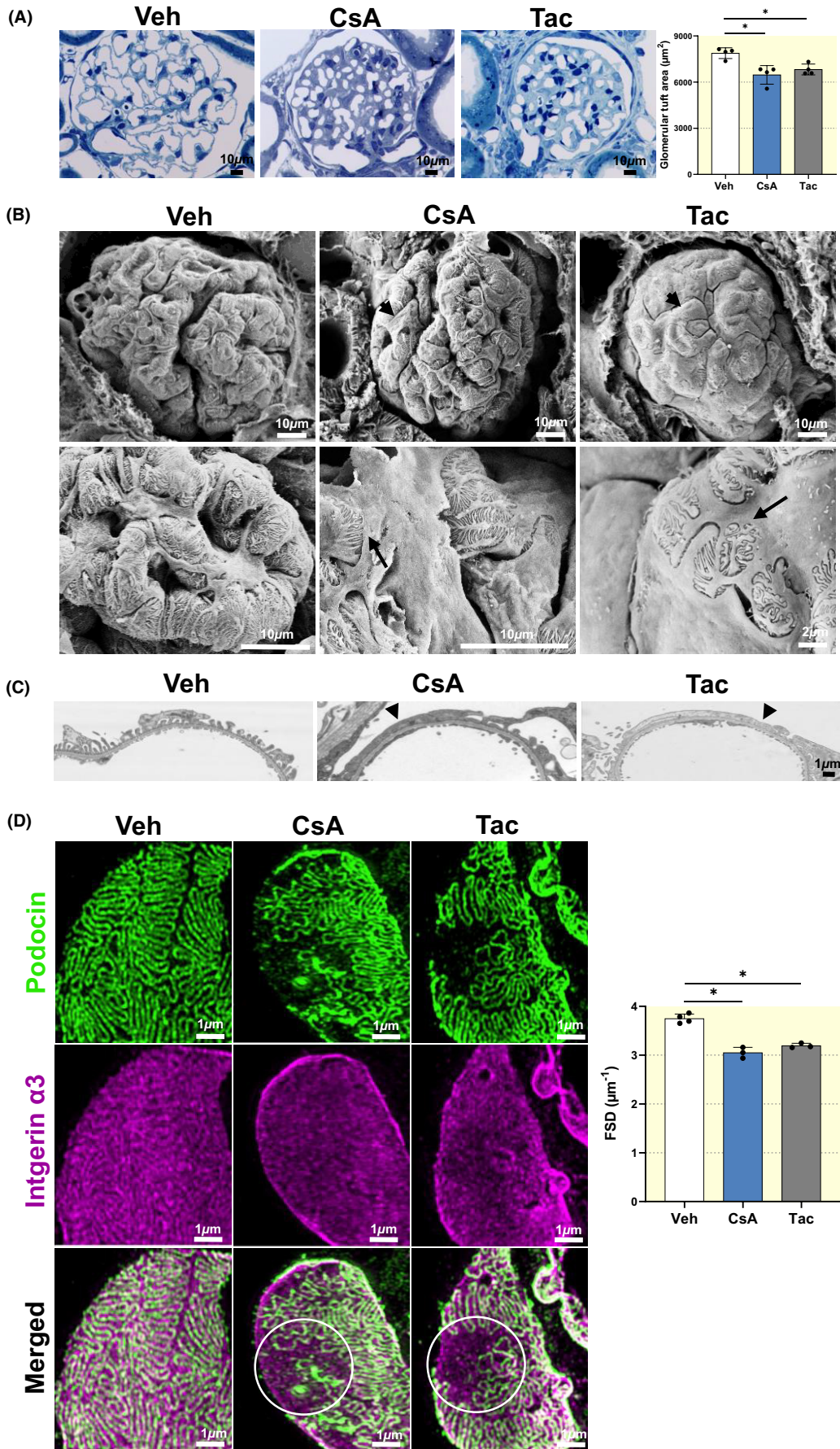
Interlobular arteries showed mild increases in wall thickness upon CNI with occasional hyaline or necrotizing subintimal or media inclusions in CsA as opposed to significant increases in intermyocyte matrix and adventitial collagen as well as myocyte thinning in Tac ([Figure S2A](#)). Glomerular afferent arterioles showed PAS-positive wall inclusions in both CNI and increased wall-to-lumen ratio in Tac (1.7-fold, $p < 0.001$; [Figure S2B,C](#)). Endothelial CD31 expression showed mildly increased signal in CsA and Tac; luminal occlusion was generally not observed ([Figure S2D](#)). Ultrastructurally, myocytes were particularly rich in contractile apparatus of single-layered media in CsA, but flattened and layered in Tac ([Figure S2E](#)). Terminal afferent arterioles regularly displayed hypergranularity of the juxtaglomerular granular cells with both treatments, with renin signal intensities increased 7-fold in CsA and 8.8-fold in Tac compared to controls ($p < 0.001$). Specifically, in the Tac group layers of granular cells featured narrowing of the afferent arteriole focally at the glomerular entry ([Figure S3A,B](#)). TEM detail of granular cells was inconspicuous in CsA but showed glycogen accumulations, necrosis, or hyaline formations in Tac ([Figure S3C](#)). Interlobular veins and ascending vasa recta viewed by SEM were normal in CsA but strikingly revealed partial or total loss of fenestrae in Tac. Focally adhering CD45-positive leukocytes were control level in CsA, but frequent in Tac ([Figure S4](#)).

3.4 | Glomeruli

Glomeruli with mild sclerosis and/or retraction were found in both groups in association with fibrotic foci.

Capillaries were narrowed, and the mesangium mildly expanded. Mean tuft area, quantified from podocin-immunostained sections, was decreased in CNI compared to Veh (−17% in CsA, −14% in Tac; $p < 0.05$; [Figure 2A](#)). Degenerative changes of the glomerular tuft varied with the degree of retraction and podocyte effacement. By SEM, focal podocyte effacement was commonly found in CsA, whereas in Tac, more extensive or generalized effacement with major podocyte degeneration was detected ([Figure 2B](#)). TEM confirmed higher podocyte effacement in Tac than in CsA ([Figure 2C](#)). FSD analysis showed that besides areas of normal configuration of the slit diaphragm, sites of significant FSD reduction, indicating effacement, were detected in both CNI groups (−18% in CsA, −15% in Tac; $p < 0.05$; [Figure 2D](#)). Ultrastructure of the capsule revealed an activated parietal epithelium with occasional vacuolization, cell height varying between 0.2 up to 4 μm , extensive granular and hyaline matrix formation, layering of the basement membrane, and adjacent hyaline or granular matrix formations particularly in CsA; synechiae with podocytes were commonly found in both CNI groups ([Figure S5A](#)). CD44 immunostaining specified its activated state by sharp increases in parietal epithelial signal in CsA and Tac; pericapsular interstitium was mildly (CsA) or substantially (Tac) infiltrated by CD45-positive leukocytes ([Figure S5B,C](#)). Endothelial fenestration of the glomerular capillaries showed conspicuous reductions in pore density by SEM which were markedly stronger in Tac than in CsA ([Figure 3A](#)), and pore size was reduced in both CNI. These changes were confirmed by TEM, revealing also substantial condensation of endothelial cells chiefly in Tac ([Figure 3B](#)). Areas of reduced pore formation were commonly facing those of podocyte effacement. Reductions in pore density were numerically confirmed (−31% in CsA, −49% in Tac; $p < 0.001$; [Figure 3C](#)). Changes in tuft structure were further paralleled by diminished WT1 immunoreactivity in Tac (−20%; $p < 0.001$; [Figure 4A](#)). Cell death-associated DNA fragmentation within the tuft by TUNEL immunofluorescence was highly increased in the Tac, but

FIGURE 2 Glomerular structure. (A) Representative glomeruli, semithin sections, Richardson's stain. Glomerular tuft size is reduced in the CNI-treated samples. Graph shows numerical evaluation ($n = 4$); means \pm SD; $*p < 0.05$. (B) Representative SEM of glomerular tufts as viewed from the urinary space after removal of Bowman's capsule. Note single capillaries with flattened podocytes (arrowhead) and retracted or fused foot processes (arrow) in CsA compared to generalized effacement of podocytes with broad cell bodies and rarified foot processes in Tac. (C) Representative TEM images of the filtration barrier. Note foot process effacement in the CsA and Tac samples (arrowheads). (D) Filtration slit density (FSD) was determined by 3D-structured illumination microscopy and Podocyte Exact Morphology Measurement Procedure; double-immunostaining with anti-podocin antibody to label the filtration slit and anti-integrin $\alpha 3$ antibody to label the glomerular basement membrane. Flat sections of capillary loops reveal sites of effacement in CsA and Tac (white circles in the merge images) by missing slit diaphragm of portions otherwise reactive for integrin $\alpha 3$. Graph shows numerical evaluation ($n = 3-4$); means \pm SD; $*p < 0.05$. Bars indicate magnification.



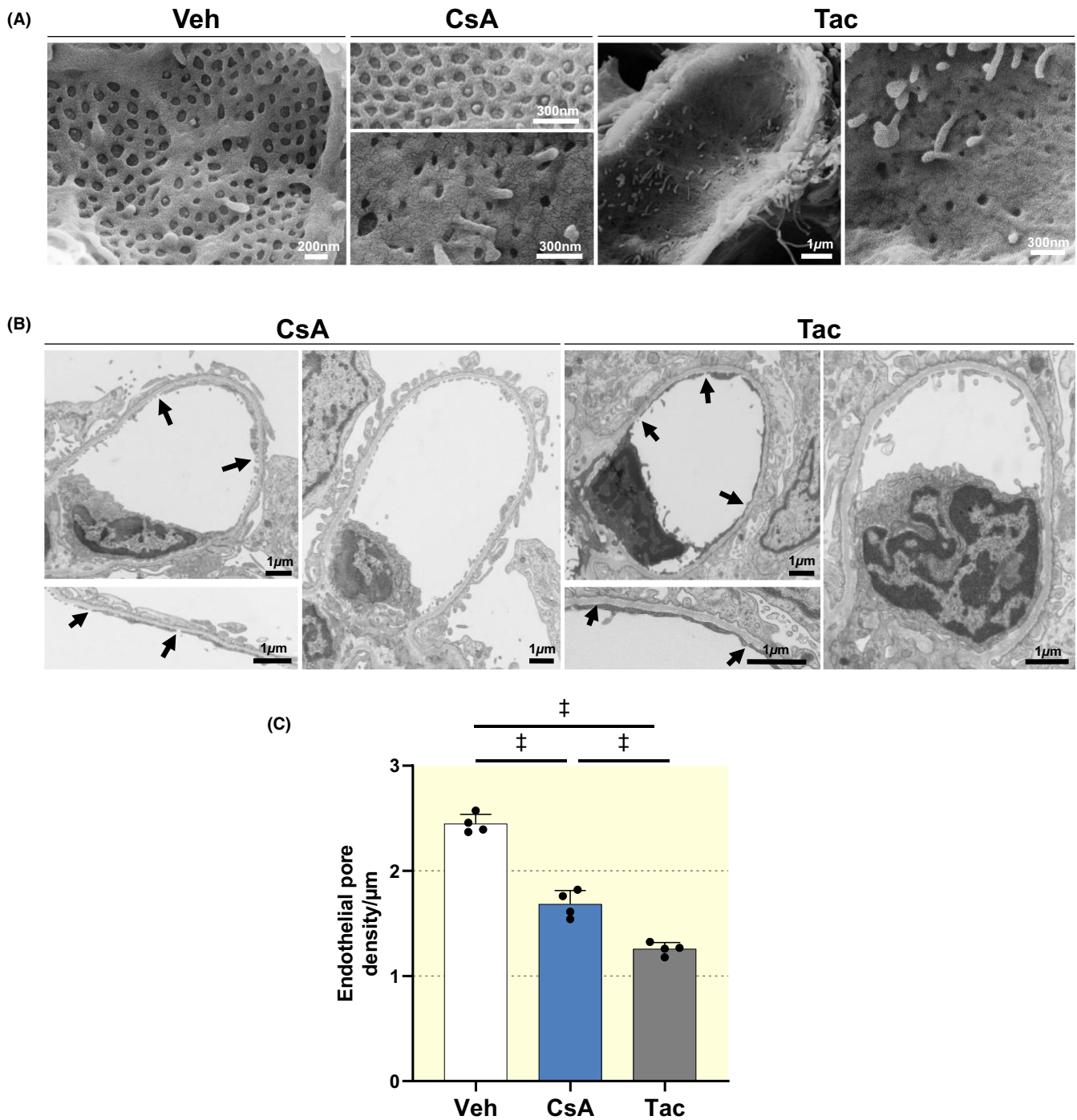


FIGURE 3 Glomerular capillaries—endothelial pore density. (A) Representative SEM images of glomerular capillary endothelial structure. Normal (top) or reduced pore density (below) in cyclosporine A (CsA). Strongly diminished pore density in tacrolimus (Tac) (overview, left image; detail, right). Note also smaller pore size in the CNi-treated samples. (B) TEM showing characteristic capillary endothelial structure in CsA; capillaries with (between arrows, upper left image) and without obvious pore losses (right). Detail (lower left) is from another capillary. In Tac, capillaries with (between arrows; upper and lower left images) and without pore losses (right) are detectable in parallel. Note striking condensation and darkening of endothelium when displaying pore losses. Bars indicate magnification. (C) Endothelial pore density per μm of glomerular basement membrane quantified from TEM sections ($n=4$); means \pm SD; $\ddagger p < 0.001$.

less so in the CsA group (10-fold in CsA, 22-fold in Tac; $p < 0.001$; **Figure 4B**); contrastingly, parietal epithelial cells showed a stronger signal in CsA than in

Tac (26-fold in CsA, $p < 0.001$, 13-fold in Tac, $p < 0.01$; **Figure 4B**). These observations were confirmed by numerical quantification (**Figure 4C**).

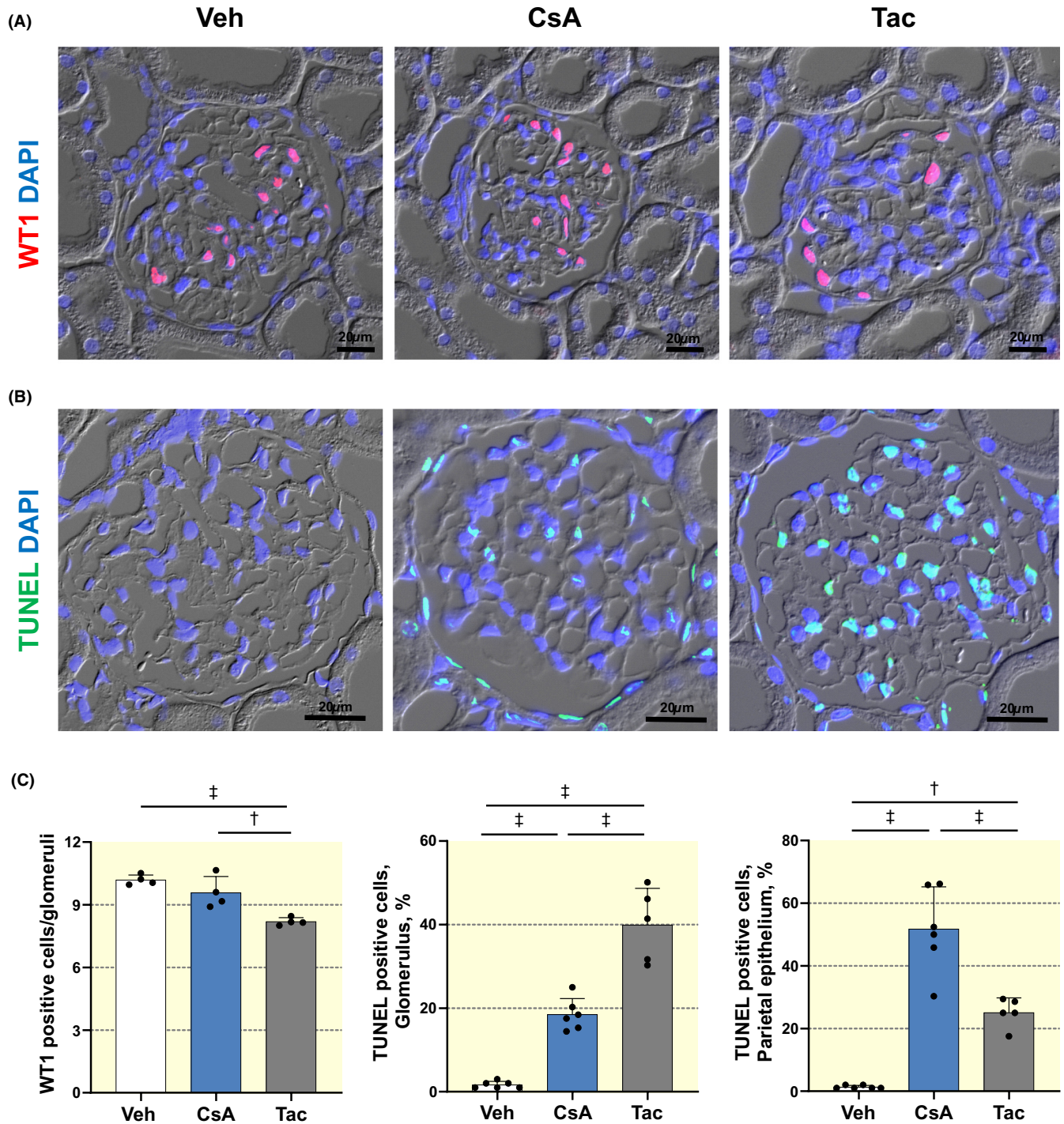


FIGURE 4 Glomerular Wilms tumor 1 protein (WT1) expression and TUNEL labeling. (A) Anti-WT1 immunoreactivity in podocyte nuclei. (B) TUNEL immunofluorescence in glomeruli. Glomerular tuft and parietal epithelium show signals in cyclosporine A (CsA) and tacrolimus (Tac). DIC optics, DAPI nuclear stain; bars indicate magnification. (C) Quantification of signals ($n=4-6$); means \pm SD; † $p < 0.01$; ‡ $p < 0.001$.

3.5 | Proximal tubule

A variety of early changes in PCT were registered upon CNI administration. In CsA, typical Richardson's dark-stained lysosomes were largely absent from PCT but instead, one to several large heteromorphic vacuoles or heterolysosomes

as well as autofluorescent residual bodies were commonly detected per area. The vacuoles reached nuclear size or beyond and were filled with PAS-positive content. In Tac, dark-stained lysosomes prevailed but were less numerous than in Veh, and heteromorphic vacuoles were rare. Lysosomal changes were quantified (decreases in dark

lysosomes –79% in CsA, –23% in Tac; increase in hetero-lysosomes 62-fold in CsA; $p < 0.001$; [Figure 5A,B](#)). By TEM, membrane-bound heteromorphic vacuoles, focally opening into the cytosol or anastomosing with other lysosomes, residual bodies with granular content, and late endosomes were identified ([Figure 5C](#)). Stages of lysosomal fusion with residual bodies and late endosomes as well as luminal exocytosis were frequent ([Figure S6A](#)). This was confirmed by SEM, showing the highest numbers of cast-like remainders of lysosomal exocytosis within the brush border membrane (BBM) of CsA samples ([Figure S6B](#)). The lysosomal nature of the heteromorphic vacuoles was identified by lysosomal associated membrane protein 1 (LAMP1) immunoreactivity forming a luminescent ring along each late endosomal/lysosomal perimeter in the CNI groups ([Figure 5D](#)). Abundance of catalase as an indicator of defense against oxidative stress was elevated in CsA compared to Veh, whereas in Tac there was no difference (1.5-fold increase in CsA, $p < 0.05$; [Figure S7A,B](#)). Ultrastructurally, major clusters of peroxisomes were located in the basal cell aspect ([Figure S7C](#)). Western blots showed significant increases for immunoreactive catalase in CsA, but not in Tac (2.3-fold increase in CsA, $p < 0.001$; [Figure S7D](#)). TUNEL immunofluorescence showed clear maxima of nuclear signals in PCT and proximal straight tubule (PST) in CsA as opposed to few scattered signals registered in Tac (PCT, increases 33-fold in CsA, $p < 0.001$, 4.8-fold in Tac, $p < 0.01$; PST, 17-fold increase in CsA, $p < 0.001$; [Figure 6A–C](#)). Further progression to necrosis affected proximal segments in both groups with losses of brush border and basolateral foldings, mitophagy, and basement membrane thickening. Whole-cell autophagy was more pronounced in CsA, whereas higher liposome accumulations were characteristic in Tac ([Figure S8A–C](#)).

3.6 | Changes in cortical interstitial vasculature

Intact tissue areas of the CsA and Tac groups showed regular peritubular capillary CD31 signal, whereas in

fibrotic foci, numerous strongly CD31-positive capillaries of a rounded, sprouting type were detected ([Figure 7A](#)). Increases of CD31 abundance in CNI groups were confirmed by Western blot analysis (increases 1.6-fold in CsA, $p < 0.01$, 1.8-fold in Tac, $p < 0.05$; [Figure 7B](#)). Changes in endothelial fenestration were observed by TEM. CNI diminished the pore density significantly in Tac (–44%, $p < 0.001$), and endothelial swelling or ridge formation was detected particularly in Tac ([Figure 7C](#)).

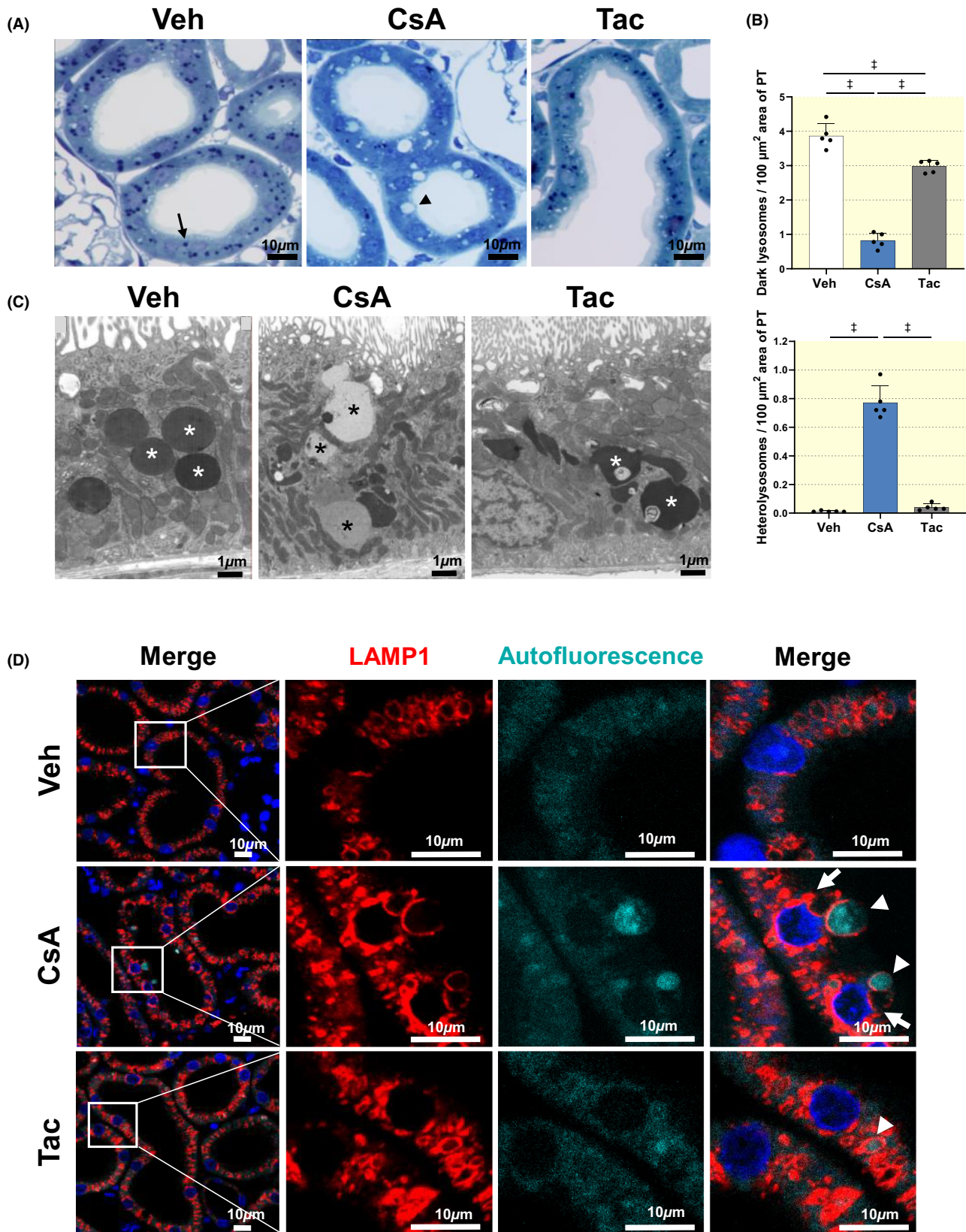
3.7 | Overview of histopathological changes

An overview of CNI-related changes in rat kidney, highlighting the differential effects between the drugs used, is shown in [Table 2](#).

3.8 | Comparative analysis in human renal biopsies with CNI nephrotoxicity

Human kidney biopsies from patients receiving CNI for maintenance immunosuppression were comparatively analyzed. Tissues from renal and nonrenal allograft recipients revealed clear signs of CNI nephrotoxicity ([Figure S9A](#)). Specifically, thickening of the glomerular basement membrane was observed in both CNI by electron microscopy. In Tac, numerically reduced endothelial pore density coincided with focal podocyte effacement ([Figure S9B,C](#)). In the proximal tubules, augmented hetero-lysosomes, luminal exocytosis and loss of BBM in PCT were focally observed in the CsA cohort ([Figure S9D,E](#)). Peritubular capillaries showed intact structure and endothelial fenestration in CsA, but altered structure and markedly reduced fenestration in Tac ([Figure S9F,G](#)). Pathological grading of morphological features confirmed substantial nephropathy (Banff 2019; score 0–3), but showed no significant differences between CNI ([Figure S9H](#)). These results did not differ between recipients of renal or nonrenal allografts.

FIGURE 5 Lysosomal changes in proximal convoluted tubule. (A) Richardson's staining, semithin sections. Proximal convoluted tubule (S1 and S2 segments) shows well-preserved standard morphology in vehicle (Veh) with dark-blue stained lysosomes (arrow) per sectioned cell. Cyclosporine A (CsA) presents with large, clear hetero-lysosomes (arrowhead) and tacrolimus (Tac) with diminished number of dark lysosomes. (B) Quantification of dark-stained lysosomes (top) and hetero-lysosomes (bottom) ($n = 5$); means \pm SD; $\ddagger p < 0.001$. (C) TEM; apical vesicular compartment, endosomes, fields of dense apical tubules, lysosomes (asterisks), and autophagic vesicles with membranous content are normally developed in Veh. Note multiple hetero-lysosomes (asterisks) forming chains in apico-basal orientation in CsA. In Tac, note multiform lysosomes with heterogenous inclusions in Tac (asterisks). (D) Anti-Lysosomal-associated membrane protein 1 (LAMP1) immunofluorescence of lysosomal stages; boxes in overviews show details on the right; note large hetero-lysosomes with LAMP1-positive perimeters irrespective of autofluorescent (arrowheads) or non-autofluorescent content (arrows) in CsA; both selected hetero-lysosomes are in the process of luminal exocytosis. In Tac, large hetero-lysosomes and autofluorescent inclusions are rare (arrowhead). DAPI nuclear stain. Bars indicate magnification.



3.9 | Multiomics analyses

RNA-seq transcriptomic, global proteomic, and phosphoproteomic analyses served to obtain mechanistic

perspectives underlying CNI-induced pathology in the rat study. Principal component analysis (PCA) and volcano graphs reveal the similarities and differences between groups (Figure S10). RNA-seq identified 1003 DEGs (507

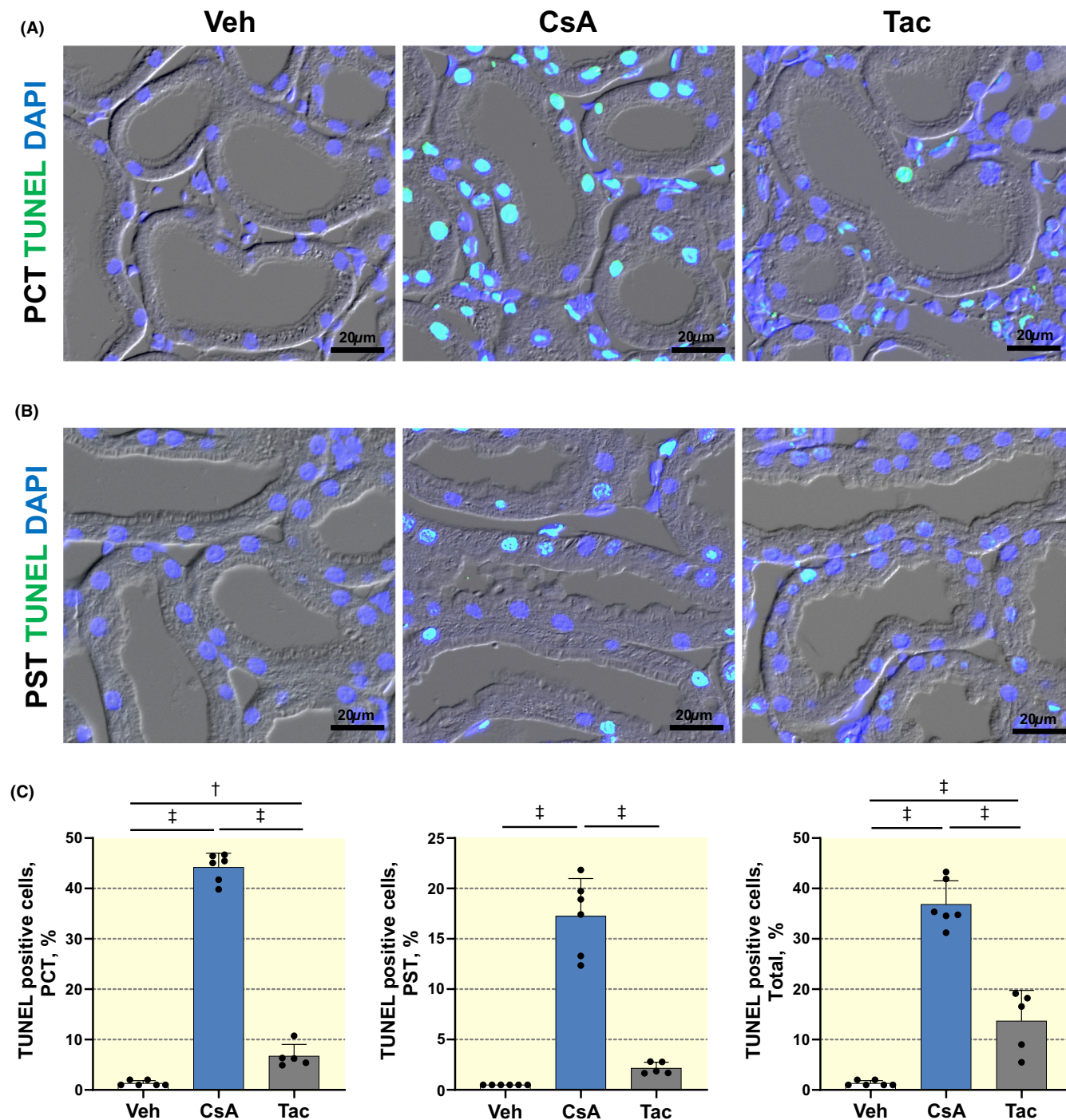


FIGURE 6 Proximal tubular TUNEL labeling. (A, B) TUNEL immunofluorescence shows blue nuclear signal in representative images. Note strong and frequent signal in cyclosporine A (CsA) and weak scattered signal in tacrolimus (Tac) proximal convoluted tubule (PCT; A). Similar results in proximal straight tubule (PST) with less signal density in CsA (B). DIC optics, DAPI nuclear stain; bars indicate magnification. (C) Quantitative evaluation; total kidney TUNEL signal is shown for comparison. Percent of total nuclei counts ($n=5-6$); means \pm SD; † $p < 0.01$; ‡ $p < 0.001$.

up- and 496 downregulated, adjusted $p < 0.1$) in CsA and 323 (105 up- and 218 downregulated, adjusted $p < 0.1$) in Tac. Global proteomics revealed 115 DEPs (52 up- and 63 downregulated) in CsA and 269 (199 up- and 70 downregulated) in Tac. Quantitative phosphoproteomic analysis discovered 64 DEPPs (46 up- and 18 downregulated,

FDR < 0.5) in CsA and 59 (35 up- and 24 were downregulated, FDR < 0.5) in Tac. Few products were jointly altered, among them increased renin and decreased calbindin (Venn diagrams in Figure 8). Pathway enrichment analysis of CNI-induced DEGs by Enrichr indicated that among others, *vasculature development*, *glomerular visceral*

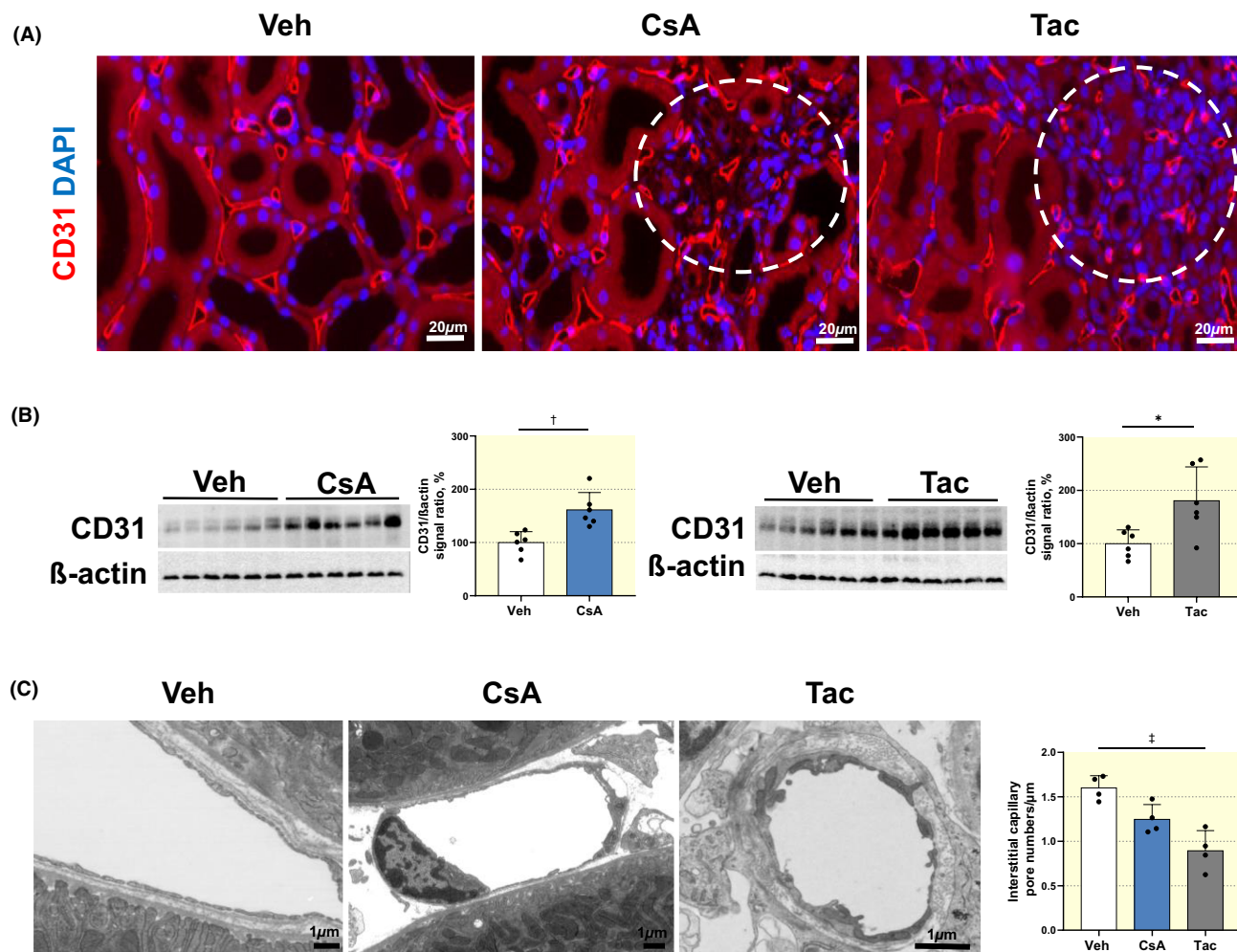


FIGURE 7 Changes in cortical interstitial vasculature. (A) Anti-CD31 immunofluorescence localized to peritubular capillaries. Note strongly positive capillaries of a rounded, sprouting type in fibrotic foci from cyclosporine A (CsA) and tacrolimus (Tac) samples (encircled areas); DAPI nuclear blue staining. (B) Western blot CD31 signals (110 kDa) from kidney extracts of CsA and Tac and their respective vehicle (Veh) groups; β-Actin (42 kDa) serves as loading control ($n=6$ per group). Densitometric evaluations on the right; means \pm SD; * $p < 0.05$; † $p < 0.01$. (C) TEM of cortical interstitial capillaries in fibrotic foci. Note sprouting type capillaries with absent fenestrae in CsA and Tac, and endothelial swelling or ridge formation particularly in Tac. Endothelial pore density per μm of capillary basement membrane quantified from TEM sections ($n=4$); means \pm SD; ‡ $p < 0.001$. Bars indicate magnification.

epithelial cell differentiation, actin cytoskeleton organization, eukaryotic translation termination, and apoptotic process were upregulated, whereas proximal tubule transport and likely associated metabolism were downregulated, supporting CsA-typical damages. In Tac, renin-angiotensin system, biological oxidations, oxidative stress-induced senescence, blood vessel endothelial cell proliferation involved in sprouting angiogenesis, and vascular wound healing were up-, and vasculature development, positive regulation of endothelial cell proliferation, mTORC1 signaling, AMPK signaling pathway, and actin filament organization downregulated, which agreed with Tac-typical structural alterations (Figure 9). Both proteomic and phosphoproteomic data were consistent with these pathways and further selectively pointed to markedly upregulated unfolded protein response pathway in CsA but not in Tac; the

respective products were verified by WB (p-PERK, 26-fold; p-IRE1 6.8-fold; sXBP1, 5.4-fold, ccasp-3, 4-fold increases in CsA, $p < 0.001$; Figures S11–S13). Among single, differentially regulated products, PDIA5 and phosphorylated PERK (*Eif2ak3*), related with UPR, as well as HMGB1 and CTSD, both regulatory in autophagy, were upregulated in CsA. In Tac, *Prkce*, *Prkd1*, *Ptger4*, and *Cav1* transcripts, CAV1 and DDAH2 proteins, and phosphorylated PRKD1, and VEGFR2 (KDR) protein, all involved in endothelial function and vasculature changes, were downregulated. We validated decreased VEGF/VEGFR2 expression in Tac by RT-PCR (*Vegf*, -15% ; *Vegfr2*, -29% ; $p < 0.05$) and WB (VEGFR2, -30% ; $p < 0.01$; Figure S14). Likewise, SYNPO transcript and protein, PALLD transcript and phosphorylation, PODXL protein, and CD2AP phosphorylation, all relevant in podocyte biology, were decreased

TABLE 2 Overview of histopathological changes.

Compartments	CNI-induced changes	Group comparison	Key figure
General	Fibrosis	CsA = Tac	Figure 1D
	Inflammation	CsA = Tac	Figure S1C
Vasculature	Arterial hyalinosis	CsA > Tac	Figure S2A
	Arterial myocyte change	CsA < Tac	Figure S2E
	Wall-to-lumen ratio	CsA < Tac	Figure S2B
	Enhanced endothelial CD31	CsA = Tac	Figure 7B
	Enhanced renin expression	CsA = Tac	Figure S3A
	Loss of fenestration, veins & capillaries	CsA < Tac	Figure S4A
	Leukocyte adhesion, veins	CsA < Tac	Figure S4B
	VEGF/VEGFR	CsA > Tac	Figure S14
Glomerulus	Glomerular tuft retraction	CsA = Tac	Figure 2A
	Podocyte effacement, TEM	CsA < Tac	Figure 2C
	Podocyte synechiae	CsA = Tac	Figure S5A
	Capsular activation, CD44	CsA = Tac	Figure S5B
	Capsular activation, CD45	CsA < Tac	Figure S5C
	Loss of fenestration	CsA < Tac	Figure 3A
	WT1 positive cells, tuft	CsA > Tac	Figure 4A
	TUNEL positive cells, tuft	CsA < Tac	Figure 4B
Proximal tubule	Lysosomal changes	CsA > Tac	Figure 5A
	Residual bodies, exocytosis	CsA > Tac	Figure S6A
	Catalase/ peroxisomes	CsA > Tac	Figure S7A
	Necrotic end stages	CsA = Tac	Figure S8C

Note: Overview of CNI-related histopathological changes, their differential effects between the drugs used, and the key Figures showing the effect. =, no change; >, major compared to; <, minor compared to.

in Tac (Table S3). Finally, we used the published list of 193 proximal tubule-specific genes identified in rat kidney to compare with the present changes.³⁵ Here, 100 differentially regulated genes (20 up- and 80 downregulated) were

altered in CsA, but only 33 genes (25 up- and 8 downregulated) in Tac, confirming the more substantial changes in CsA compared to Tac (Figure S15).

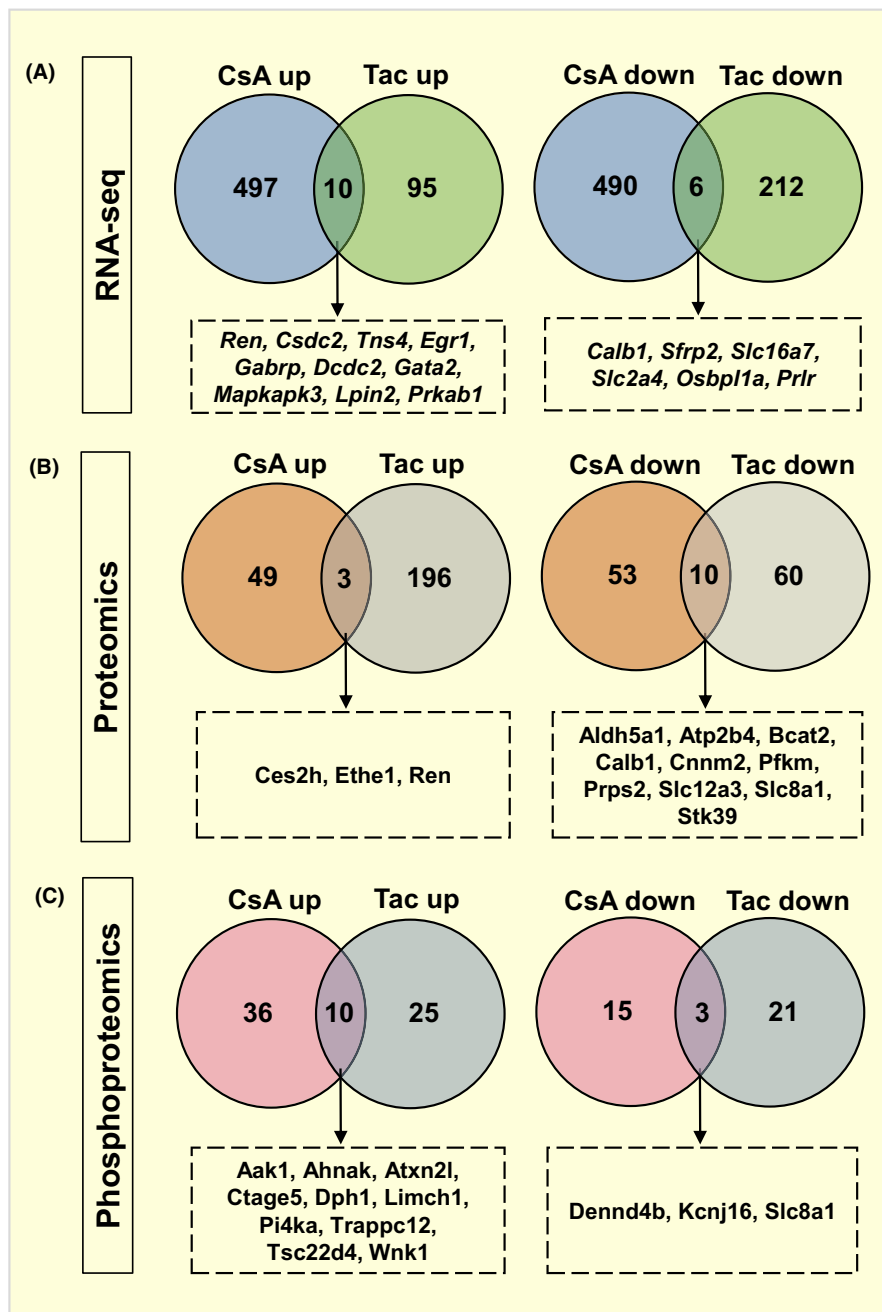
4 | DISCUSSION

This study presents distinctive pathogenesis for CsA versus Tac. Responses to treatments thus associated CsA with a tubular and Tac with a microvascular focus. Principal landmarks of CNI pathology affecting all renal compartments are otherwise reflected. The different damage patterns offer perspectives to adapt human immunosuppressive protocols to patients' history thereby lessening nephrotoxic damage. Although lesion characteristics were confirmed in human renal biopsy samples, our study focuses on CNI nephropathy under early chronic conditions without obvious comorbidities in the rat. High-resolution histopathology, candidate mRNA and protein assessments as well as comprehensive multiomics attributed renal microenvironmental remodeling to novel, specific protein signatures.

Histological alterations point to distinct pathogenesis in rat arteriolar wall changes between CNI used, probably mirroring early phase condition, whereas clinical data report arteriolar hyalinization to similar extent at late stage.³ In our model, greater RAAS stimulation in Tac versus CsA may be among the causes in early phase.^{13,36} Disproportionate impairment of vasodilatory prostaglandins in Tac agrees with the observed downregulated Ep4 receptor (*Ptger4*) and related PGE2 action, implying less eNOS function.^{37,38} *Prkce* mRNA, selectively downregulated in Tac, may suggest impaired VEGF signaling, since its knockdown in bovine endothelial cells abrogates VEGF-stimulated AKT phosphorylation, decreases action of its cognate receptor VEGFR2, and impairs VEGF-stimulated NOS activity.³⁹ Likewise, *CAV1* mRNA & protein were downregulated in Tac but not in CsA, supporting related NO deficiency downstream of impaired VEGF signaling.⁴⁰ Selective upregulation of *DDAH2*, which degrades endogenous NOS inhibitors, indicate potential compensation to preserve NO availability in Tac.⁴¹ Increased leukocyte adhesion, more in Tac than in CsA, pointed to affection of the endothelial surface and agreed with focal incidence of CD45-positive cell accumulations.⁴² This difference is in line with CsA's beneficial effects on adhesion molecules in vitro.⁴³ Stimulated endothelial CD31 in both conditions suggests a cytoprotective response to altered shear stress^{44,45} and/or adjustment for leukocyte transmigration.⁴⁶

In humans, overt arteriolar hyalinosis and resulting blood flow reduction up to 80% normally associates with glomerular damage without difference between CNI

FIGURE 8 Differentially expressed genes, proteins, and phosphoproteins. (A–C) Venn diagrams showing the number of differentially expressed genes, proteins, and phosphoproteins (RNA-seq and proteomics, adjusted $p < 0.1$; phosphoproteomics, FDR < 5 ; CNI vs. Veh). Jointly regulated products are listed in box. “up,” upregulated; “down,” downregulated.



used.³ The rat study commonly revealed retraction of the tuft and fibrotic alterations of Bowman's capsules in early and advanced foci with both CNI. Pronounced CD44 expression, as found in the activated parietal epithelium, is a useful marker for early CNI nephrotoxicity also in human grafts.⁴⁷ In conjunction with fibrous podocyte synechia and CD45-positive inflammatory cell accumulations these features suggested early stages of sclerotic lesions.^{48,49} Tuft retraction, likely resulting from diminished microvascular perfusion,⁵⁰ and decreased FSD occurred to similar extent in CsA and Tac. Proteinuria was still not detected, which may be related with the decrease in GFR; also, podocyte albumin storage was strongly decreased in CNI, pointing at its reduced filtration (not shown). Clearly, however,

endothelial fenestration is affected more by Tac than CsA in glomerular as well as peritubular capillaries and renal veins, and results in the human Tac cohort were confirmatory. VEGF signaling involvement appears possible due to its effects on pore density in conjunction with TNF α signaling in mice.⁵¹ A human microvascular CNI nephrotoxicity model further underscores VEGF's potential role. That model displays reduced fenestration and VEGF signaling along with stimulated *Adamts1* and cytoplasmic deteriorations.⁵² Accordingly, we find exacerbated endothelial cytoplasm condensation for Tac. *Adamts1* and transcription factor *Sox17* are likewise stimulated. *Sox17* status differed between our groups and may provide compensatory endothelial repair in CsA, yet failing to do so in

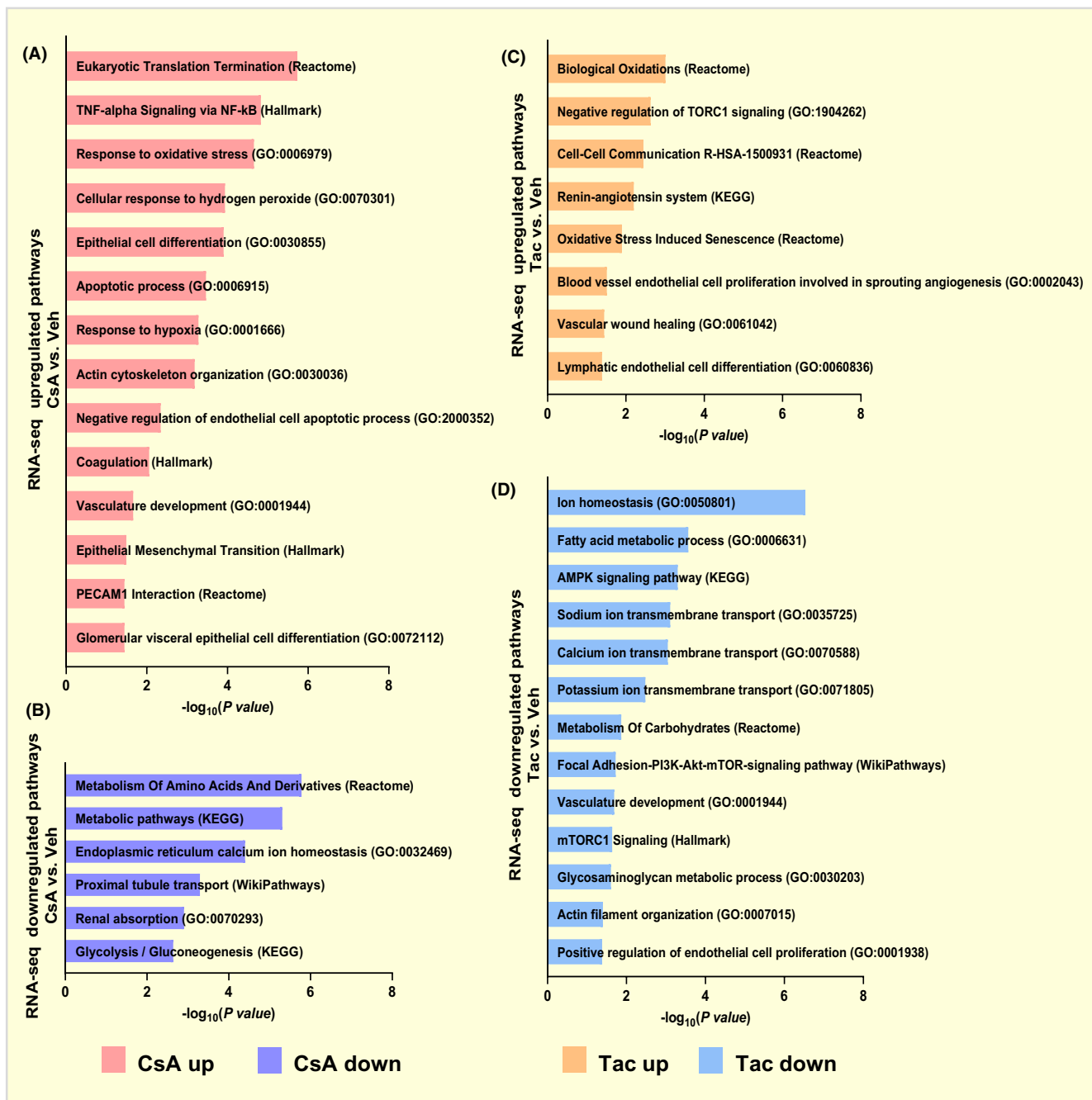


FIGURE 9 Pathway enrichment analysis of differentially expressed genes affected by CNI treatments. Treatment with cyclosporine A (CsA) and tacrolimus (Tac) leads to different molecular pathway responses in chronic CNI nephrotoxicity. Significantly enriched pathways in genes upregulated (A) and downregulated (B) in CsA versus vehicles ($p < 0.05$). Significantly enriched pathways in genes upregulated (C) and downregulated (D) in Tac versus vehicles ($p < 0.05$). Term lists used in this analysis were GO_Biological_Processes, WikiPathways, Reactome, KEGG, and Hallmark to determine enriched processes and pathways from differentially expressed genes (Enrichr webtool).

Tac.⁵³ With caveolin-1 (*Cav1*) substantially diminished at the mRNA and protein level in Tac, our multiomics data further link reduced angiogenesis to pore formation.^{54,55} This is further supported by protein kinase D1 (PRKD1) mRNA and phosphorylation being selectively downregulated in Tac. PRKD1 also controls VEGFR2, downregulated in Tac, by disinhibiting transcription factor AP2.⁵⁶ Extensive foot process effacement in Tac, more than in

CsA, suggests impaired filtration barrier and hydraulic conductivity, since capillary segments with advanced pore rarefaction show parallel podocyte effacement. This agrees with decreased WT1 and increased TUNEL signals in podocytes, both exacerbated in Tac. Diminution of WT1, an established marker of podocytes, is associated with barrier function loss⁵⁷ and early changes toward glomerulosclerosis,⁵⁸ while enhanced TUNEL signals relate

to apoptosis or repair.⁵⁹ Key podocyte genes such as palladin, CD2AP, synaptopodin, nephronectin, and podocalyxin, all intrinsic structural components of podocytes, were selectively downregulated in Tac which also underscores higher podocyte damage compared to CsA, and concomitant impairment in shape and motility of their foot processes.^{60,61} Associated decrease in phosphorylation of CD2AP, a stabilizing protein of the slit diaphragm, at Ser 404 may reflect further loss of function.⁶² Although in their longitudinal histological cohort study, Nankivell et al. reported equal glomerular damage scores in CsA and Tac samples,³ our results suggest glomerular vulnerability to Tac at an early stage.

Tubular damage in CNI nephropathy has been extensively discussed in the past, yet it has remained uncertain whether downstream effects of affected vasculature, glomerular malfunction, or direct toxicity to epithelia prevail at its origin. The proximal tubule has earlier been considered to be the principal nephron segment affected by CsA and Tac, with no distinction.^{63,64} In contrast, our data suggests substantial differences in proximal tubular damage. The major finding is massive accumulation of heterolysosomes, identified by their LAMP1-positive boundaries, and their exocytotic luminal extrusion predominantly in the CsA group, whereas changes in Tac were much less lysosomal-based. PERK, a key regulator in the UPR, was markedly increased together with the UPR transducer IRE1 and downstream spliced XBP1. These canonical cascades likely prompted cleaved caspase-3 and related apoptosis shown here for CsA, but not for Tac.^{18,65} Already before, we and others reported impaired proteostasis leading to proapoptotic ER stress upon CsA, but not for Tac.^{17,20} Several lines point to the localization of these particular pathways in the proximal tubule. Among them are the TUNEL signal and related apoptotic cell features.^{20,65} With the UPR response also driving regulation of TFEB, an acknowledged master regulator of autophagy and lysosomal biogenesis,⁶⁶ CsA may block autophagic flux, thus causing the selective lysosomal disorder that was not observed in Tac. Notably, mTOR inhibitors, commonly employed in combination with CNI, may have a beneficial effect herein through their activation of TFEB.^{22,66,67} Stimulated *Arl8b*, expression standing for enhanced lysosomal exocytosis, was observed in the proximal tubule in CsA, supported the lysosome-based defect.⁶⁸ Upregulated HMGB1 and CTSD indicate bioenergetic maladaptation and mitochondrial dysfunction along with enhanced autophagy in CsA.^{64,69,70} Such disorders may arise with oxidative stress, since CsA stimulated catalase with activated proximal tubular peroxisomes.⁷¹

It is therefore reasonable to conclude that CsA-related cytotoxicity, among other sites, preferentially affects

these proximal tubule tissue components. Comparison of our DEG signatures with published library data referring to the proximal tubule support this interpretation (Figure S15). The presented changes typically began at the urinary pole and affected the entire length of PCT, but had little structural manifestation in PST. This is unlike early findings in the rat upon higher CsA dosage, combination with low salt diet, and shorter treatment suggesting the PST as the primary target for CsA toxicity.⁶³ Cell death in PCT was markedly higher in CsA than in Tac, but more advanced damage features suggested similar loss of proximal tubular differentiation in either group.

Lesions in the human cohorts typically reflected long-term CNI nephrotoxicity with the known, comparable arteriolar toxicity and glomerulosclerosis,³ but also confirmed our observations on differential patterns in epithelia and capillary walls.

In summary, we show distinctive pathogenic patterns arising in renal compartments under CsA versus Tac medications. Besides common effects like fibrosis and atrophy, landmark differences were the predominant affections of the filtration barrier in Tac and of the PCT in CsA. Protein signatures from selective probing and multiomics analysis point at the mechanisms involved. For Tac, these include perturbed VEGF/VEGFR2 signaling, while cytotoxic UPR signaling and altered autophagic flux are more prominent for CsA. Should this translate into clinical settings, future CNI selection may consider more selectively lesions of the renal compartments in conjunction with risk factors for damage of the filtration barrier versus the proximal convoluted tubule.

AUTHOR CONTRIBUTIONS

Hasan Demirci: conceptualization; data curation; formal analysis; investigation; methodology; software; validation; visualization; writing—original draft; and writing—review & editing. **Suncica Popovic:** data curation; formal analysis; investigation; methodology; and visualization. **Carsten Dittmayer:** data curation; formal analysis; methodology; resources; software; and visualization. **Duygu Elif Yilmaz:** data curation; formal analysis; investigation; and validation. **Ismail Amr El-Shimy:** data curation; formal analysis; and software. **Michael Mülleder:** data curation; formal analysis; and software. **Christian Hinze:** formal analysis; software; and supervision. **Mingzhen Su:** data curation; methodology; and visualization. **Philipp Mertins:** data curation; methodology; and software. **Marieluise Kirchner:** data curation; methodology; and software. **Bilgin Osmanodja:** data curation and methodology. **Alexander Paliege:** conceptualization; investigation; and writing—review & editing. **Klemens Budde:** conceptualization; investigation; and writing—review & editing. **Kerstin Amann:** conceptualization;

investigation; validation; and writing—review & editing. **Pontus B. Persson:** writing—original draft and writing—review & editing. **Kerim Mutig:** conceptualization; funding acquisition; and project administration. **Sebastian Bachmann:** conceptualization; data curation; formal analysis; funding acquisition; investigation; methodology; project administration; resources; software; supervision; validation; visualization; writing—original draft; and writing—review & editing.

ACKNOWLEDGMENTS

This work was financially supported by Deutsche Forschungsgemeinschaft BA700/22-2, MU2924/2-2, and SFB 1365-C04/-S01. HD was supported by a doctoral fellowship from Ministry of National Education, Turkey. We thank Hermann-Josef Gröne, Wilhelm Kriz, David Ellison, and Richard Warth for constructive advice, Anette Drobbe for secretarial help, Kerstin Riskowsky, Katja Dörfel, Ariane Anger for expert technical help, Sara Timm, Petra Schrade, and John Horn (Core Facility for Electron Microscopy) for microscopical help, Junda Hu, Erdmann Seeliger, Nicole and Tim Endlich (NIPOKA, Greifswald, Germany) for methodological help in 3D-SIM, and Lukasz Szyrwił, and Nils Blüthgen for bioinformatic data analysis. Open Access funding enabled and organized by Projekt DEAL.

CONFLICT OF INTEREST STATEMENT

The authors have declared that no conflict of interest exists.

DATA AVAILABILITY STATEMENT

EM large-scale digitization data are available under www.nanotome.org repository. The RNA-seq data sets are available from the Gene Expression Omnibus repository under the following accession numbers: GSE225215. Proteomic and phosphoproteomic data sets are available via ProteomeXchange with identifier PXD038841, PXD038546, respectively.

ORCID

Hasan Demirci  <https://orcid.org/0000-0001-7730-9653>
 Suncica Popovic  <https://orcid.org/0000-0002-3121-7953>
 Duygu Elif Yilmaz  <https://orcid.org/0000-0002-1110-8389>

REFERENCES

- Farouk SS, Rein JL. The many faces of calcineurin inhibitor toxicity—what the FK? *Adv Chronic Kidney Dis.* 2020;27(1):56-66. doi:10.1053/j.ackd.2019.08.006
- Naesens M, Kuypers DRJ, Sarwal M. Calcineurin inhibitor nephrotoxicity. *Clin J Am Soc Nephrol.* 2009;4(2):481-508. doi:10.2215/CJN.04800908
- Nankivell BJ, P'Ng CH, O'Connell PJ, Chapman JR. Calcineurin inhibitor nephrotoxicity through the lens of longitudinal histology: comparison of cyclosporine and tacrolimus eras. *Transplantation.* 2016;100(8):1723-1731. doi:10.1097/TP.0000000000001243
- Kaufman DB, Woodle ES, Shields AR, et al. Belatacept for simultaneous calcineurin inhibitor and chronic corticosteroid immunosuppression avoidance: two-year results of a prospective, randomized multicenter trial. *Clin J Am Soc Nephrol.* 2021;16(9):1387-1397. doi:10.2215/CJN.13100820
- Wissing KM, Abramowicz D, Weekers L, et al. Prospective randomized study of conversion from tacrolimus to cyclosporine a to improve glucose metabolism in patients with posttransplant diabetes mellitus after renal transplantation. *Am J Transplant.* 2018;18(7):1726-1734. doi:10.1111/ajt.14665
- Leal R, Tsapepas D, Crew RJ, Dube GK, Ratner L, Batal I. Pathology of calcineurin and mammalian target of rapamycin inhibitors in kidney transplantation. *Kidney Int Rep.* 2018;3(2):281-290. doi:10.1016/j.ekir.2017.10.010
- Liptak P, Ivanyi B. Primer: histopathology of calcineurin-inhibitor toxicity in renal allografts. *Nat Rev Nephrol.* 2006;2(7):398-404. doi:10.1038/ncpneph0225
- Mengel M, Mihatsch M, Halloran PF. Histological characteristics of calcineurin inhibitor toxicity—there is No such thing as specificity! *Am J Transplant.* 2011;11(12):2549-2550. doi:10.1111/j.1600-6143.2011.03719.x
- Bremer S, Vethe NT, Skauby M, et al. NFAT-regulated cytokine gene expression during tacrolimus therapy early after renal transplantation: NFAT-regulated cytokine gene expression during tacrolimus therapy. *Br J Clin Pharmacol.* 2017;83(11):2494-2502. doi:10.1111/bcp.13367
- Williams CR, Gooch JL. Calcineurin inhibitors and immunosuppression—a tale of two isoforms. *Expert Rev Mol Med.* 2012;14:e14. doi:10.1017/erm.2012.8
- Blankenstein KI, Borschewski A, Labes R, et al. Calcineurin inhibitor cyclosporine a activates renal Na-K-Cl cotransporters via local and systemic mechanisms. *Am J Physiol Renal Physiol.* 2017;312(3):F489-F501. doi:10.1152/ajprenal.00575.2016
- Hoorn EJ, Walsh SB, McCormick JA, Zietse R, Unwin RJ, Ellison DH. Pathogenesis of calcineurin inhibitor-induced hypertension. *J Nephrol.* 2012;25(3):269-275. doi:10.5301/jn.5000174
- Hu J, Xu Y, Bachmann S, Mutig K. Angiotensin II receptor blockade alleviates calcineurin inhibitor nephrotoxicity by restoring cyclooxygenase 2 expression in kidney cortex. *Acta Physiol.* 2021;232(1):e13612. doi:10.1111/apha.13612
- Labes R, Brinkmann L, Kulow VA, et al. Daprodustat prevents cyclosporine-A-mediated anemia and peritubular capillary loss. *Kidney Int.* 2022;102(4):750-765. doi:10.1016/j.kint.2022.04.025
- Lazelle RA, McCully BH, Terker AS, et al. Renal deletion of 12 kDa FK506-binding protein attenuates tacrolimus-induced hypertension. *J Am Soc Nephrol.* 2016;27(5):1456-1464. doi:10.1681/ASN.2015040466
- Lamoureux F, Mestre E, Essig M, Sauvage FL, Marquet P, Gastinel LN. Quantitative proteomic analysis of cyclosporine-induced toxicity in a human kidney cell line and comparison with tacrolimus. *J Proteome.* 2011;75(2):677-694. doi:10.1016/j.jprot.2011.09.005

17. Fedele AO, Carraro V, Xie J, Averous J, Proud CG. Cyclosporin a but not FK506 activates the integrated stress response in human cells. *J Biol Chem.* 2020;295(44):15134-15143. doi:10.1074/jbc.RA120.014531
18. Cybulsky AV. Endoplasmic reticulum stress, the unfolded protein response and autophagy in kidney diseases. *Nat Rev Nephrol.* 2017;13(11):681-696. doi:10.1038/nrneph.2017.129
19. Pallet N, Bouvier N, Bendjallabah A, et al. Cyclosporine-induced endoplasmic reticulum stress triggers tubular phenotypic changes and death. *Am J Transplant.* 2008;8(11):2283-2296. doi:10.1111/j.1600-6143.2008.02396.x
20. Yilmaz DE, Kirschner K, Demirci H, Himmerkus N, Bachmann S, Mutig K. Immunosuppressive calcineurin inhibitor cyclosporine a induces proapoptotic endoplasmic reticulum stress in renal tubular cells. *J Biol Chem.* 2022;298(3):101589. doi:10.1016/j.jbc.2022.101589
21. Klawitter J, Klawitter J, Schmitz V, et al. Low-salt diet and cyclosporine nephrotoxicity: changes in kidney cell metabolism. *J Proteome Res.* 2012;11(11):5135-5144. doi:10.1021/pr300260e
22. Li Z, An N, Huang X, et al. Cyclosporine a blocks autophagic flux in tubular epithelial cells by impairing TFEB-mediated lysosomal function. *J Cell Mol Med.* 2021;25(12):5729-5743. doi:10.1111/jcmm.16593
23. Mayrdorfer M, Liefeldt L, Wu K, et al. Exploring the complexity of death-censored kidney allograft failure. *J Am Soc Nephrol.* 2021;32(6):1513-1526. doi:10.1681/ASN.2020081215
24. Budde K, Prashar R, Haller H, et al. Conversion from calcineurin inhibitor- to Belatacept-based maintenance immunosuppression in renal transplant recipients: a randomized phase 3b trial. *J Am Soc Nephrol.* 2021;32(12):3252-3264. doi:10.1681/ASN.2021050628
25. Unnersjö-Jess D, Ramdedovic A, Höhne M, et al. Three-dimensional super-resolved imaging of paraffin-embedded kidney samples. *Kidney360.* 2022;3(3):446-454. doi:10.34067/KID.0005882021
26. Siegerist F, Ribback S, Dombrowski F, et al. Structured illumination microscopy and automatized image processing as a rapid diagnostic tool for podocyte effacement. *Sci Rep.* 2017;7(1):11473. doi:10.1038/s41598-017-11553-x
27. Dittmayer C, Goebel HH, Heppner FL, Stenzel W, Bachmann S. Preparation of samples for large-scale automated electron microscopy of tissue and cell ultrastructure. *Microsc Microanal.* 2021;27(4):815-827. doi:10.1017/S1431927621011958
28. Müller T, Kalxdorf M, Longuespée R, Kazdal DN, Stenzinger A, Krijgsveld J. Automated sample preparation with SP 3 for low-input clinical proteomics. *Mol Syst Biol.* 2020;16(1):e9111. doi:10.15252/msb.20199111
29. Demichev V, Messner CB, Vernardis SI, Lilley KS, Ralser M. DIA-NN: neural networks and interference correction enable deep proteome coverage in high throughput. *Nat Methods.* 2020;17(1):41-44. doi:10.1038/s41592-019-0638-x
30. Zhang X, Smits AH, van Tilburg GB, Ovaa H, Huber W, Vermeulen M. Proteome-wide identification of ubiquitin interactions using UbIA-MS. *Nat Protoc.* 2018;13(3):530-550. doi:10.1038/nprot.2017.147
31. Mertins P, Mani DR, Ruggles KV, et al. Proteogenomics connects somatic mutations to signalling in breast cancer. *Nature.* 2016;534(7605):55-62. doi:10.1038/nature18003
32. Tyanova S, Temu T, Cox J. The MaxQuant computational platform for mass spectrometry-based shotgun proteomics. *Nat Protoc.* 2016;11(12):2301-2319. doi:10.1038/nprot.2016.136
33. Andoh TF, Burdmann EA, Fransechini N, Houghton DC, Bennett WM. Comparison of acute rapamycin nephrotoxicity with cyclosporine and FK506. *Kidney Int.* 1996;50(4):1110-1117. doi:10.1038/ki.1996.417
34. Klawitter J, Klawitter J, Kushner E, et al. Association of Immunosuppressant-Induced Protein Changes in the rat kidney with changes in urine metabolite patterns: a Proteo-metabonomic study. *J Proteome Res.* 2010;9(2):865-875. doi:10.1021/pr900761m
35. Lee JW, Chou CL, Knepper MA. Deep sequencing in micro-dissected renal tubules identifies nephron segment-specific transcriptomes. *J Am Soc Nephrol.* 2015;26(11):2669-2677. doi:10.1681/ASN.2014111067
36. Wang X, Jiang S, Fei L, et al. Tacrolimus causes hypertension by increasing vascular contractility via RhoA (Ras homolog family member a)/ROCK (rho-associated protein kinase) pathway in mice. *Hypertension.* 2022;79(10):2228-2238. doi:10.1161/HYPERTENSIONAHA.122.19189
37. Hristovska AM, Rasmussen LE, Hansen PBL, et al. Prostaglandin E₂ induces vascular relaxation by E-Prostanoid 4 receptor-mediated activation of endothelial nitric oxide synthase. *Hypertension.* 2007;50(3):525-530. doi:10.1161/HYPERTENSIONAHA.107.088948
38. Purdy KE, Arendshorst WJ. EP₁ and EP₄ receptors mediate prostaglandin E₂ actions in the microcirculation of rat kidney. *Am J Physiol Renal Physiol.* 2000;279(4):F755-F764. doi:10.1152/ajprenal.2000.279.4.F755
39. Rask-Madsen C, King GL. Differential regulation of VEGF signaling by PKC- α and PKC- ϵ in endothelial cells. *Arterioscler Thromb Vasc Biol.* 2008;28(5):919-924. doi:10.1161/ATVBAHA.108.162842
40. Sonveaux P, Martinive P, DeWever J, et al. Caveolin-1 expression is critical for vascular endothelial growth factor-induced ischemic hindlimb collateralization and nitric oxide-mediated angiogenesis. *Circ Res.* 2004;95(2):154-161. doi:10.1161/01.RES.0000136344.27825.72
41. Baylis C. Nitric oxide deficiency in chronic kidney disease. *Am J Physiol Renal Physiol.* 2008;294(1):F1-F9. doi:10.1152/ajprenal.00424.2007
42. Gallego MJ, Zoja C, Morigi M, et al. Cyclosporine enhances leukocyte adhesion to vascular endothelium under physiologic flow conditions. *Am J Kidney Dis.* 1996;28(1):23-31. doi:10.1016/S0272-6386(96)90126-2
43. Markovic S, Raab M, Daxecker H, Griesmacher A, Karimi A, Müller MM. In vitro effects of cyclosporin a on the expression of adhesion molecules on human umbilical vein endothelial cells. *Clin Chim Acta.* 2002;316(1-2):25-31. doi:10.1016/S0009-8981(01)00732-X
44. Cheung K, Ma L, Wang G, et al. CD31 signals confer immune privilege to the vascular endothelium. *Proc Natl Acad Sci USA.* 2015;112(43):E5815-E5824. doi:10.1073/pnas.1509627112
45. Wang H, Riha GM, Yan S, et al. Shear stress induces endothelial differentiation from a murine embryonic mesenchymal progenitor cell line. *Arterioscler Thromb Vasc Biol.* 2005;25(9):1817-1823. doi:10.1161/01.ATV.0000175840.90510.a8

46. Sluiter TJ, van Buul JD, Huvencers S, Quax PHA, de Vries MR. Endothelial barrier function and leukocyte transmigration in atherosclerosis. *Biomedicine*. 2021;9(4):328. doi:[10.3390/biomedicines9040328](https://doi.org/10.3390/biomedicines9040328)
47. Hayashi A, Okamoto T, Nio-Kobayashi J, et al. CD44 as a pathological marker for the early detection of calcineurin inhibitor-induced nephrotoxicity post kidney transplantation. *Biomed Res*. 2022;43(5):181-186. doi:[10.2220/biomedres.43.181](https://doi.org/10.2220/biomedres.43.181)
48. Bernhardt A, Fehr A, Brandt S, et al. Inflammatory cell infiltration and resolution of kidney inflammation is orchestrated by the cold-shock protein Y-box binding protein-1. *Kidney Int*. 2017;92(5):1157-1177. doi:[10.1016/j.kint.2017.03.035](https://doi.org/10.1016/j.kint.2017.03.035)
49. Kuppe C, Gröne HJ, Ostendorf T, et al. Common histological patterns in glomerular epithelial cells in secondary focal segmental glomerulosclerosis. *Kidney Int*. 2015;88(5):990-998. doi:[10.1038/ki.2015.116](https://doi.org/10.1038/ki.2015.116)
50. Kim JH, Lee YH, Lim BJ, Jeong HJ, Kim PK, Shin JI. Influence of cyclosporine a on glomerular growth and the effect of mizoribine and losartan on cyclosporine nephrotoxicity in young rats. *Sci Rep*. 2016;6(1):22374. doi:[10.1038/srep22374](https://doi.org/10.1038/srep22374)
51. Xu C, Chang A, Hack BK, Eadon MT, Alper SL, Cunningham PN. TNF-mediated damage to glomerular endothelium is an important determinant of acute kidney injury in sepsis. *Kidney Int*. 2014;85(1):72-81. doi:[10.1038/ki.2013.286](https://doi.org/10.1038/ki.2013.286)
52. Nagao RJ, Marcu R, Shin YJ, et al. Cyclosporine induces fenestra-associated injury in human renal microvessels *in vitro*. *ACS Biomater Sci Eng*. 2022;8(1):196-207. doi:[10.1021/acsbomaterials.1c00986](https://doi.org/10.1021/acsbomaterials.1c00986)
53. Liu M, Zhang L, Marsboom G, et al. Sox17 is required for endothelial regeneration following inflammation-induced vascular injury. *Nat Commun*. 2019;10(1):2126. doi:[10.1038/s41467-019-10134-y](https://doi.org/10.1038/s41467-019-10134-y)
54. Tahir SA, Park S, Thompson TC. Caveolin-1 regulates VEGF-stimulated angiogenic activities in prostate cancer and endothelial cells. *Cancer Biol Ther*. 2009;8(23):2284-2294. doi:[10.4161/cbt.8.23.10138](https://doi.org/10.4161/cbt.8.23.10138)
55. Satchell SC, Braet F. Glomerular endothelial cell fenestrations: an integral component of the glomerular filtration barrier. *Am J Physiol Renal Physiol*. 2009;296(5):F947-F956. doi:[10.1152/ajprenal.90601.2008](https://doi.org/10.1152/ajprenal.90601.2008)
56. Wang Y, Hoepfner LH, Angom RS, et al. Protein kinase D up-regulates transcription of VEGF receptor-2 in endothelial cells by suppressing nuclear localization of the transcription factor AP2 β . *J Biol Chem*. 2019;294(43):15759-15767. doi:[10.1074/jbc.RA119.010152](https://doi.org/10.1074/jbc.RA119.010152)
57. Guo JK. WT1 is a key regulator of podocyte function: reduced expression levels cause crescentic glomerulonephritis and mesangial sclerosis. *Hum Mol Genet*. 2002;11(6):651-659. doi:[10.1093/hmg/11.6.651](https://doi.org/10.1093/hmg/11.6.651)
58. Asfahani RI, Tahoun MM, Miller-Hodges EV, et al. Activation of podocyte notch mediates early Wt1 glomerulopathy. *Kidney Int*. 2018;93(4):903-920. doi:[10.1016/j.kint.2017.11.014](https://doi.org/10.1016/j.kint.2017.11.014)
59. Moore CL, Savenka AV, Basnakian AG. TUNEL assay: a powerful tool for kidney injury evaluation. *Int J Mol Sci*. 2021;22(1):412. doi:[10.3390/ijms22010412](https://doi.org/10.3390/ijms22010412)
60. Artelt N, Ludwig TA, Rogge H, et al. The role of Palladin in podocytes. *J Am Soc Nephrol*. 2018;29(6):1662-1678. doi:[10.1681/ASN.2017091039](https://doi.org/10.1681/ASN.2017091039)
61. Menon R, Otto EA, Berthier CC, et al. Glomerular endothelial cell-podocyte stresses and crosstalk in structurally normal kidney transplants. *Kidney Int*. 2022;101(4):779-792. doi:[10.1016/j.kint.2021.11.031](https://doi.org/10.1016/j.kint.2021.11.031)
62. Tossidou I, Teng B, Worthmann K, et al. Tyrosine phosphorylation of CD2AP affects stability of the slit diaphragm complex. *J Am Soc Nephrol*. 2019;30(7):1220-1237. doi:[10.1681/ASN.2018080860](https://doi.org/10.1681/ASN.2018080860)
63. Mihatsch MJ, Kyo M, Morozumi K, Yamaguchi Y, Nickenleit V, Ryffel B. The side-effects of ciclosporine-a and tacrolimus. *Clin Nephrol*. 1998;49(6):356-363.
64. Zmijewska AA, Zmijewski JW, Becker EJ Jr, Benavides GA, Darley-Usmar V, Mannon RB. Bioenergetic maladaptation and release of HMGB1 in calcineurin inhibitor-mediated nephrotoxicity. *Am J Transplant*. 2021;21(9):2964-2977. doi:[10.1111/ajt.16561](https://doi.org/10.1111/ajt.16561)
65. Han SW, Li C, Ahn KO, et al. Prolonged endoplasmic reticulum stress induces apoptotic cell death in an experimental model of chronic cyclosporine nephropathy. *Am J Nephrol*. 2008;28(5):707-714. doi:[10.1159/000127432](https://doi.org/10.1159/000127432)
66. Franco-Juárez B, Coronel-Cruz C, Hernández-Ochoa B, et al. TFEB; beyond its role as an autophagy and lysosomes regulator. *Cells*. 2022;11(19):3153. doi:[10.3390/cells11193153](https://doi.org/10.3390/cells11193153)
67. Silva HT Jr, Cibrik D, Johnston T, et al. Everolimus plus reduced-exposure CsA versus mycophenolic acid plus standard-exposure CsA in renal-transplant recipients. *Am J Transplant*. 2010;10(6):1401-1413. doi:[10.1111/j.1600-6143.2010.03129.x](https://doi.org/10.1111/j.1600-6143.2010.03129.x)
68. Wu PH, Onodera Y, Giaccia AJ, et al. Lysosomal trafficking mediated by Arl8b and BORC promotes invasion of cancer cells that survive radiation. *Commun Biol*. 2020;3(1):620. doi:[10.1038/s42003-020-01339-9](https://doi.org/10.1038/s42003-020-01339-9)
69. Di YQ, Han XL, Kang XL, et al. Autophagy triggers CTSD (cathepsin D) maturation and localization inside cells to promote apoptosis. *Autophagy*. 2021;17(5):1170-1192. doi:[10.1080/1548627.2020.1752497](https://doi.org/10.1080/1548627.2020.1752497)
70. Tang D, Kang R, Livesey KM, et al. Endogenous HMGB1 regulates autophagy. *J Cell Biol*. 2010;190(5):881-892. doi:[10.1083/jcb.200911078](https://doi.org/10.1083/jcb.200911078)
71. Godin N, Liu F, Lau GJ, et al. Catalase overexpression prevents hypertension and tubular apoptosis in angiotensinogen transgenic mice. *Kidney Int*. 2010;77(12):1086-1097. doi:[10.1038/ki.2010.63](https://doi.org/10.1038/ki.2010.63)

SUPPORTING INFORMATION

Additional supporting information can be found online in the Supporting Information section at the end of this article.

How to cite this article: Demirci H, Popovic S, Dittmayer C, et al. Immunosuppression with cyclosporine versus tacrolimus shows distinctive nephrotoxicity profiles within renal compartments. *Acta Physiol*. 2024;240:e14190. doi:[10.1111/apha.14190](https://doi.org/10.1111/apha.14190)